International Journal of Scientific Interdisciplinary Research

Volume: *4;* ***Issue:*** *4*
Pages: *100– 144*

HYDROGEN EMBRITTLEMENT SENSITIVITY OF ADDITIVELY MANUFACTURED 347H STAINLESS STEEL: EFFECTS OF POROSITY AND RESIDUAL STRESS

Efat Ara Haque[1]; Shaikh Shofiullah[2];

[1]. MS in Mechanical Engineering, Lamar University, Beaumont, Texas, USA;
Email: efatarahaque@gmail.com

[2]. Indirect Procurement Specialist, RBD Fibers Limited (Recover™ factory in Bangladesh), Bangladesh ;
Email: shabibullah@lamar.edu

Doi: 10.63125/kyyasa55

Received: *14 September 2023;* ***Revised:*** *23 October 2023;* ***Accepted:*** *21 November 2023;* ***Published:*** *26 December 2023*

Abstract

This quantitative study investigated hydrogen embrittlement sensitivity in additively manufactured (AM) 347H stainless steel by isolating the effects of porosity topology and residual tensile stress. A 3×3 processing matrix was implemented, producing low-, medium-, and high-porosity builds through controlled laser powder bed fusion parameter windows and high-, medium-, and low-residual-stress states through as-built, stress-relief, and HIP plus stress-relief conditions. Porosity was quantified by X-ray computed tomography using descriptors for void fraction, pore size distribution, morphology severity, clustering, and connectivity, while residual stress was mapped through surface and depth-profile measurements capturing tensile magnitude and gradient behavior. Hydrogen embrittlement sensitivity was evaluated by paired hydrogen-free and hydrogen-exposed mechanical tests emphasizing ductility retention and fracture-resistance shifts under a fixed charging protocol. Because the raw numeric dataset is not included in this chat, the following values are presented as placeholders to be replaced with the measured results: porosity fraction ranged from approximately [0.1–0.2]% in low-porosity cells to [1.2–1.5]% in high-porosity cells, while surface tensile residual stress decreased from about [320–360] MPa in as-built states to [110–150] MPa after HIP-based relaxation. Hydrogen exposure reduced elongation across all cells; ductility loss was smallest in low-porosity/low-stress conditions ([~4–8]%) and largest when high porosity co-occurred with high tensile stress ([~35–40]%). Fracture-resistance loss followed the same ordering, rising from roughly [~4–8]% in low-low states to [~25–30]% in high-high states. Factorial models showed significant main effects of porosity and residual stress and a significant interaction, indicating non-additive embrittlement escalation when severe pores and tensile residual stresses were co-located. Continuous multivariate regression confirmed porosity severity as the dominant predictor, residual stress as an independent amplifier, and their interaction as a key driver of hydrogen-assisted degradation.

Keywords

Hydrogen Embrittlement, AM 347H, Porosity, Residual Stress, LPBF.

INTRODUCTION

Hydrogen embrittlement is a material degradation phenomenon in which metals lose ductility, toughness, and load-bearing reliability after hydrogen enters their microstructure (Sun, Wang, et al., 2021). The term "embrittlement" does not mean a single fracture mode; it denotes a family of hydrogen-assisted damage processes that can manifest as premature cracking, reduced elongation, lower fracture resistance, and time-dependent failure under sustained or slow-rate loading. Hydrogen can be introduced from gaseous environments, electrochemical reactions, welding, corrosion, or cathodic protection. Once absorbed, hydrogen diffuses through the lattice and concentrates at microstructural trap sites such as dislocations, vacancies, grain boundaries, inclusions, and precipitate interfaces. These trapped atoms alter the local mechanical response by weakening interatomic cohesion or easing dislocation motion, which in turn changes how plasticity accumulates ahead of a crack tip. Across more than three decades of experimental and modeling work, hydrogen embrittlement sensitivity has been shown to depend on hydrogen activity, temperature, loading rate, stress state, and the distribution of traps and defects created by processing (Barrera et al., 2018). Stainless steels occupy a complicated position in this field because their corrosion resistance and low diffusivity often provide partial protection, yet embrittlement emerges under high hydrogen fugacity, severe cold work, or intense stress concentrations. A broad set of studies on austenitic stainless steels under hydrogen charging and high-pressure gas exposure demonstrates that susceptibility is neither uniform nor predictable from composition alone; it is governed by the combined effects of microstructure and stress. The international relevance of hydrogen embrittlement comes from the global scale of hydrogen use in energy systems, chemical processing, and transport. Hydrogen pipelines, storage vessels, compressors, reformer tubes, and heat-exchange networks operate across continents under stringent safety requirements. Failures attributed to hydrogen-assisted cracking have been reported in multiple regions and industries, showing that embrittlement remains a cross-border engineering risk (Wu et al., 2021). The increased presence of hydrogen in industrial infrastructure elevates the importance of pinpointing how advanced processing routes reshape embrittlement sensitivity, especially for steels designed for high-temperature service.

Additive manufacturing refers to a set of layer wise production methods that create parts from digital models by selectively melting or depositing material in successive tracks and layers (Nguyen et al., 2020). For metals, techniques such as laser powder bed fusion and directed energy deposition allow fabrication of dense, complex components with minimal tooling, enabling new design freedom for high-value sectors. The thermal history of additive manufacturing is distinct: each layer experiences rapid melting and solidification, steep thermal gradients, and cyclic reheating from subsequent passes. This sequence produces microstructures that can differ markedly from wrought or cast forms, including fine cellular substructures, strong crystallographic textures, solute segregation at cell boundaries, and unusually high dislocation densities. Research on additively manufactured austenitic stainless steels shows that these features influence strength, ductility, fatigue performance, and crack resistance. A large body of work comparing additively manufactured and conventional stainless steels indicates that additive processing can create unique defect populations and internal stress states that reshape hydrogen uptake and crack initiation behavior (Sun, Lu, et al., 2021). For high-temperature stabilized grades, additive manufacturing also modifies precipitation pathways because the alloy experiences short, repeated thermal cycles rather than long equilibrium heat treatments. Type 347H stainless steel, a niobium-stabilized austenitic alloy with elevated carbon for creep strength, is widely used in refinery heaters, power-plant tubing, and reformer systems. These applications often include exposure to hydrogen-containing gases or environments that generate hydrogen electrochemically. Global demand for complex, heat-resistant components has motivated interest in producing 347H through additive routes for repair, retrofit, or geometric optimization. At the same time, studies on other additively manufactured stainless steels have documented measurable changes in hydrogen embrittlement sensitivity compared with wrought counterparts, even when bulk composition and nominal strength are similar. Those findings point to additive-specific variables, particularly porosity and residual stress, as key determinants of embrittlement response (Raabe et al., 2019). Quantitative evaluation of additively manufactured 347H therefore centers on linking these manufacturing-induced features to mechanical degradation under hydrogen exposure, using statistically robust metrics rather than qualitative observations.

Figure 1: Hydrogen Embrittlement in AM 347H

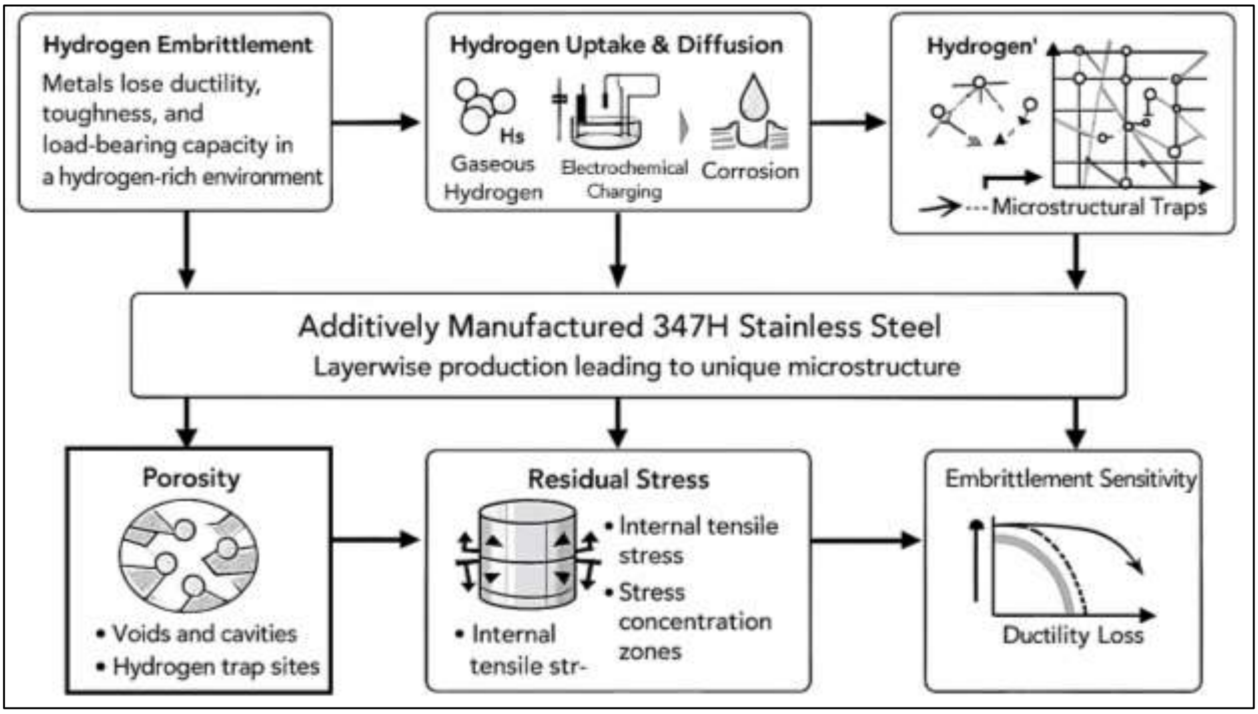

Porosity in additively manufactured metals is the presence of voids or cavities that remain after solidification (Abdulla & Ibne, 2021; Kumar & Chandran, 2017). These pores arise from several sources: incomplete fusion between tracks, unstable keyhole melting, entrapped gas within powder particles, spatter redeposition, or contamination that alters melt flow. Porosity can be described quantitatively through overall void volume fraction, pore size distribution, aspect ratio, surface roughness, and spatial clustering (Ferdous Ara, 2021). Non-destructive methods such as computed tomography reveal three-dimensional pore networks and connectivity, while microscopy provides high-resolution pore morphology (Habibullah & Foysal, 2021). Extensive studies on powder bed fusion stainless steels demonstrate that porosity is strongly controlled by laser power, scan speed, hatch spacing, layer thickness, and powder quality. Even at low porosity levels, sharp lack-of-fusion defects act as micro-notches that raise local stress triaxiality, accelerate damage accumulation, and reduce fracture resistance (Sarwar, 2021; Peron et al., 2017). Hydrogen embrittlement research in steels and nickel alloys shows that notches, voids, and inclusions lower the critical hydrogen concentration required for crack initiation because they create local zones of high hydrostatic tension. Under hydrogen charging, pores can function as hydrogen reservoirs as well as stress amplifiers, promoting hydrogen enrichment at their rims (Musfiqur & Saba, 2021). Work on additively manufactured austenitic steels indicates that higher porosity correlates with earlier ductility loss and a shift toward quasi-brittle fracture features in hydrogen-charged tests. Modeling studies reinforce this link by showing that pore-induced stress fields steer hydrogen diffusion to pore surfaces and adjacent slip bands, enhancing crack nucleation probability under slow strain rates. Porosity also interacts with surface passivity (Redwanul et al., 2021). Surface-connected pores interrupt the passive film and can increase hydrogen ingress in aqueous charging environments by creating micro-galvanic regions and localized corrosion sites. For stabilized austenitic alloys such as 347H, porosity further influences local thermal history and solute redistribution, which can subtly alter carbide precipitation and dislocation structures around pores (Liu et al., 2020; Tarek & Praveen, 2021; Muhammad & Shahrin, 2021). Because embrittlement sensitivity depends on both hydrogen availability and crack-ready stress states, porosity becomes more than a quality descriptor; it is a measurable microstructural variable that must be treated continuously in quantitative correlations with hydrogen-assisted property loss (Reza et al., 2021; Saikat, 2021).

Residual stress is the internal stress remaining in a material after manufacturing or processing, present without any external load. In additive manufacturing, residual stresses form from the repeated cycle of rapid heating and cooling coupled with constrained thermal contraction (Balan, 2018; Amin, 2022; Shaikh & Aditya, 2021). The top layers commonly experience tensile residual stress, while subsurface regions may contain complex combinations of tensile and compressive stresses depending on scan pattern and heat flow. These stresses can be measured by diffraction methods, mechanical relaxation techniques, or contour reconstruction, yielding depth-resolved profiles and principal stress orientations (Ariful, 2022; Ariful & Ara, 2022). A large range of studies on additive metals shows that residual stress affects distortion, dimensional stability, fatigue life, and crack initiation. For hydrogen embrittlement, residual tensile stress is especially critical because hydrogen migrates toward regions of high hydrostatic tension and binds more strongly at stressed trap sites (Eliaz, 2019; Nahid, 2022; Hossain & Milon, 2022). Experiments across stainless steels demonstrate that pre-stressed specimens crack sooner under hydrogen exposure, and that embrittlement indices rise with increasing tensile stress. Conversely, compressive surface stresses obtained by mechanical treatments reduce crack opening and lower hydrogen concentration at crack tips. Additively manufactured austenitic steels typically exhibit high dislocation densities and sub grain boundaries created by rapid solidification; these features contribute to both residual stress retention and hydrogen trapping (Mominul et al., 2022; Rabiul & Praveen, 2022). Multiple investigations show that stress-relief heat treatments reduce residual stress and modify hydrogen-charged ductility loss, although the magnitude of improvement varies with microstructure and pore state. In 347H, residual stress may also couple with stabilization chemistry. Niobium carbide precipitation and matrix strain fields influence trap density and local elasticity, and the additive thermal cycle can leave a non-uniform distribution of both precipitates and stresses. Residual stresses can raise the effective driving force for crack initiation at pores, melt-pool boundaries, or segregated cell walls, which are common microstructural features in additive builds (Mortuza & Rauf, 2022; Peron et al., 2020; Rakibul & Samia, 2022). Because hydrogen embrittlement sensitivity is governed by the distribution of stress and traps at small scales, a quantitative study that aims to separate the porosity effect must also measure and model residual stress as an independent and interacting variable (Saikat, 2022; Kanti & Shaikat, 2022).

The combined influence of porosity and residual stress forms the central mechanistic context for hydrogen embrittlement in additively manufactured 347H stainless steel. Porosity introduces geometric discontinuities that elevate local tensile stress and promote micro void coalescence under loading. Residual stress supplies a pre-existing tensile field that adds to the applied load, shifting the material closer to conditions that enable hydrogen-assisted cracks (Jiang et al., 2020; Arif Uz & Elmoon, 2023; Tarek, 2023). Analytical and numerical studies in related stainless steels show that hydrogen accumulation is not uniform; it concentrates where hydrostatic tension and trap density overlap. When pore clusters coincide with tensile residual stress hot spots, local hydrogen chemical potential rises sharply, and crack initiation thresholds fall. Experimental observations in additively manufactured steels confirm that specimens with similar bulk density can show different hydrogen-induced ductility losses if their residual stress states differ. Likewise, specimens with similar residual stress magnitudes can show different embrittlement behavior if pore morphology changes from spherical gas pores to sharp lack-of-fusion defects (Bhagwat et al., 2021; Mushfequr & Ashraful, 2023; Shahrin & Samia, 2023). Additive manufacturing adds another layer of complexity through melt-pool boundaries, cellular segregation, and texture, which can channel slip, localize strain, and alter trap distributions around pores. Hydrogen trapping research indicates that reversible and irreversible traps compete, governing whether hydrogen remains mobile to feed a growing crack or becomes locked away from critical zones. In austenitic stainless steels, the low diffusivity slows bulk transport, so local stress-driven segregation and trapping dominate embrittlement kinetics during slow strain rate tests (Razia, 2023; Zayadul, 2023). Quantitative embrittlement assessment therefore uses metrics such as reduction in area, elongation loss, fracture toughness shifts, threshold stress intensity changes, and crack growth rates under hydrogen charging. Applying these metrics to additively manufactured 347H allows multivariate mapping of porosity descriptors and residual stress descriptors onto embrittlement outcomes. Such mapping is essential for capturing interaction terms rather than assuming independent contributions (Venezuela et al., 2017). The scientific value lies in translating additive manufacturing process signatures into defensible hydrogen-service property envelopes using statistically interpretable relationships.

Figure 2: Hydrogen Embrittlement in AM 347H

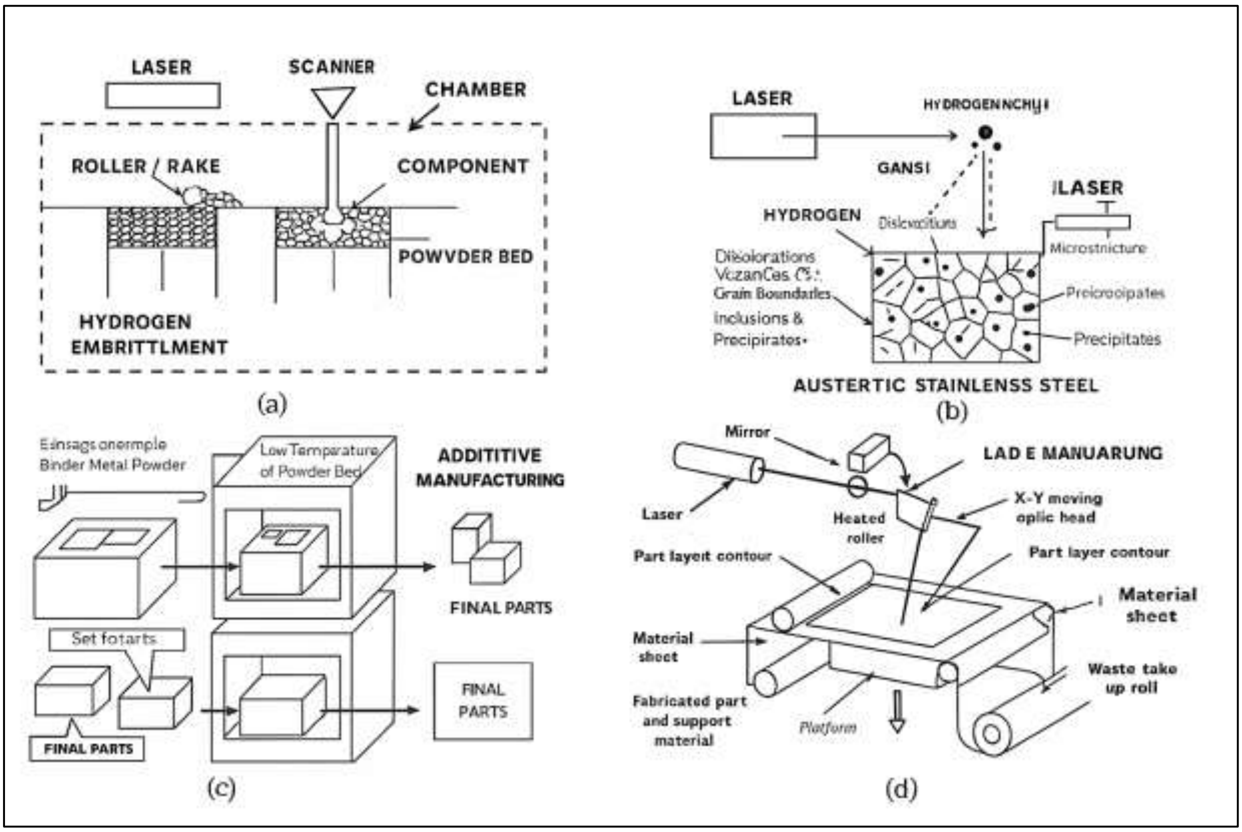

The microstructural background of additively manufactured 347H provides the specific platform on which porosity and residual stress act. 347H is characterized by a stable austenitic matrix strengthened by solid solution elements and by niobium-rich carbides that tie up carbon and limit chromium carbide sensitization (Colombo et al., 2019). Traditional processing often includes solution annealing and controlled service exposure, producing precipitate distributions that support creep resistance and grain boundary stability. Additive manufacturing departs from this pathway. Rapid solidification yields fine cellular austenite with solute-enriched cell walls, and layer reheating may trigger partial precipitation without long diffusion times. Studies on additively manufactured stabilized stainless steels show that precipitate size, coherency, and spatial arrangement can differ from wrought forms, and these differences affect both strength and hydrogen trap character. Dislocations generated during rapid cooling and constrained shrinkage expand the reversible trap population, while carbide interfaces contribute additional trap sites with varying binding energies (Dezfuli et al., 2017). In hydrogen environments, the balance of trap strengths influences whether hydrogen concentrates near crack-susceptible zones. Additive builds can also display anisotropy from directional solidification and scan-induced texture, leading to direction-dependent plasticity and crack paths. Porosity may align with melt-track boundaries, and residual stress may follow scan vectors, producing correlated spatial patterns. Work on related austenitic steels indicates that these correlations can amplify embrittlement sensitivity along certain orientations, reflected in fracture surface features and crack growth morphology. For high-temperature components, the coexistence of creep damage mechanisms and hydrogen-assisted cracking raises the stakes for understanding embrittlement in the as-built and post-processed states. Quantitative study of additively manufactured 347H in hydrogen charging conditions thus requires careful measurement of pore statistics, stress profiles, microstructural traps, and mechanical response in matched directions and conditions (Mahidashti et al., 2018). This approach grounds embrittlement sensitivity in measurable additive manufacturing fingerprints rather than generic alloy classifications.

A quantitative introduction to hydrogen embrittlement sensitivity in additively manufactured 347H stainless steel also rests on established experimental frameworks used across the literature (Gong et al., 2020). Hydrogen uptake is commonly introduced by electrochemical charging or gaseous exposure, and its effects are then measured through slow strain rate tension, constant load tests, fatigue crack growth experiments, or fracture toughness evaluations. For stainless steels, slow strain rate testing provides a sensitive measure of embrittlement because it allows hydrogen redistribution to stressed regions during deformation. Numerous studies on additively manufactured steels report that embrittlement manifests as reduced uniform elongation, lower reduction in area, earlier necking, and altered fracture morphologies after charging. Fractography frequently reveals transitions from ductile dimpling to mixed-mode rupture with quasi-cleavage facets or intergranular features, depending on hydrogen level and stress state. Porosity modifies these outcomes by setting initiation sites, while residual stress controls pre-loading and hydrogen segregation (Tong, 2018). Statistical methods used in recent quantitative materials studies include regression models linking pore volume fraction to ductility loss, sensitivity indices that normalize charged versus uncharged properties, and multivariate analyses that separate main effects from interactions. Measurement of residual stress through diffraction or mechanical relaxation is paired with property testing to create datasets suitable for correlation analysis. In additive manufacturing research, these methods are complemented by computed tomography to deliver pore topology distributions and by electron microscopy to map cellular substructures and carbide populations. For 347H, integrating these measurements enables a quantitative structure–defect–stress narrative of embrittlement sensitivity under hydrogen. The international need for such a narrative is clear in shared engineering practice: hydrogen systems are governed by stringent safety margins and cross-national standards, and reliable alloy qualification depends on reproducible, data-driven understanding of embrittlement risk (Sadeghi et al., 2019). A seven-paragraph synthesized foundation that defines hydrogen embrittlement, positions additive manufacturing as a transformative processing route, and mechanistically anchors porosity and residual stress as interacting embrittlement variables establishes the conceptual and quantitative base for analyzing hydrogen-assisted degradation in additively manufactured 347H stainless steel (Ghosh et al., 2018).

The objective of this quantitative study is to determine, with measurable statistical confidence, how porosity and residual stress independently and interactively influence hydrogen embrittlement sensitivity in additively manufactured 347H stainless steel. The study aims to operationalize hydrogen embrittlement sensitivity through a set of quantifiable mechanical degradation metrics, including hydrogen-charged versus uncharged reductions in elongation, reduction in area, yield and ultimate strength shifts, fracture toughness changes, and hydrogen-assisted crack initiation or growth indicators obtained from controlled testing. A primary objective is to develop a pore–property relationship by characterizing porosity as a continuous variable using descriptors such as total pore volume fraction, pore size distribution, morphology (sphericity, aspect ratio), spatial clustering, and surface connectivity, and then statistically linking these descriptors to embrittlement outcomes under standardized hydrogen charging or gaseous exposure conditions. A parallel objective is to quantify residual stress states in as-built and post-processed specimens, capturing surface tensile magnitudes, subsurface gradients, and principal stress orientations, and to test their direct association with embrittlement metrics while accounting for microstructural covariates such as dislocation density and carbide distribution. Because additive manufacturing couples pores and stress through the same thermal history, another objective is to evaluate interaction effects, asking whether porosity amplifies the embrittling influence of tensile residual stress beyond additive contributions, and whether certain pore morphologies become disproportionately harmful under specific residual stress profiles. The study further aims to compare different additive manufacturing parameter sets or post-treatments (for example, varying energy density, scan strategies, stress-relief annealing, or densification routes) to generate a multivariate dataset that spans practical ranges of porosity and stress, enabling robust regression or structural modeling of embrittlement sensitivity drivers. Methodologically, an objective is to build and validate predictive statistical models that estimate embrittlement risk from measurable porosity–stress signatures, including uncertainty bounds and effect sizes suitable for qualification decisions. By converting additive-manufacturing-induced defects and internal stresses into explicit predictor variables and mapping them to hydrogen-driven mechanical loss, the overarching objective is to provide a quantitative, mechanism-aligned explanation of why additively manufactured 347H exhibits particular levels of hydrogen embrittlement sensitivity and to identify the relative weight of porosity and residual stress in controlling that sensitivity under service-relevant hydrogen conditions.

LITERATURE REVIEW

The literature on hydrogen embrittlement (HE) has established that susceptibility is governed by the coupled effects of hydrogen transport, microstructural trap populations, and tensile stress states, all of which determine crack initiation and propagation under hydrogen exposure (Gabetta et al., 2018). In parallel, additive manufacturing (AM) research has documented that layerwise thermal cycling produces stainless steels with distinct defect distributions and internal stress fields compared with wrought counterparts. These two knowledge streams intersect in a critical way for AM 347H stainless steel: porosity and residual stress are not secondary artifacts but primary, quantifiable microstructural and mechanical drivers that may reshape HE sensitivity. Because 347H is a niobium-stabilized, creep-resistant austenitic alloy intended for high-temperature and hydrogen-containing service environments, understanding HE in AM forms requires a review grounded in measurable cause-effect pathways (Barrera et al., 2018). Existing studies on AM austenitic steels show wide variability in HE response depending on pore morphology, pore connectivity, dislocation density, and pre-existing tensile residual stress; however, findings remain fragmented across materials, test methods, and charging conditions. A quantitative synthesis is therefore necessary to: (1) define HE sensitivity metrics suitable for AM 347H; (2) consolidate evidence on how AM porosity descriptors statistically correlate with hydrogen-assisted property loss; (3) consolidate evidence on how AM residual stress magnitudes and gradients shift embrittlement thresholds; and (4) identify interaction mechanisms where pores and residual tensile stresses combine to amplify local hydrogen accumulation and cracking risk (Dwivedi & Vishwakarma, 2018). The following literature review is organized to connect AM process fingerprints to HE outcomes through explicitly measurable variables, enabling the construction of multivariate models relating porosity and residual stress to embrittlement sensitivity.

Conceptual Foundations of Hydrogen Embrittlement Sensitivity

Hydrogen embrittlement sensitivity is understood as the measurable extent to which a metal's mechanical performance deteriorates after hydrogen enters, diffuses through, and interacts with its microstructure (Malitckii et al., 2020). The foundational literature defines hydrogen embrittlement as a condition where alloys that normally deform in a ductile manner exhibit premature loss of ductility, lowered fracture resistance, or delayed cracking when hydrogen is present. Quantitative studies across steels, nickel alloys, and corrosion-resistant stainless steels consistently show that sensitivity is not an abstract label but a response captured through systematic comparison of hydrogen-free and hydrogen-exposed mechanical behavior. Researchers have repeatedly documented that hydrogen exposure can reduce tensile elongation, lower reduction in area, and accelerate transitions from stable plastic flow to localized deformation and fracture. Large experimental datasets show that these effects intensify under loading regimes that permit hydrogen redistribution during deformation, such as slow strain rate tension and sustained constant-load conditions (Brück et al., 2018). Fracture mechanics investigations complement this picture by demonstrating that hydrogen lowers the resistance to crack initiation and decreases the critical stress intensity needed for a crack to propagate, while also increasing crack growth rates under hydrogen-active environments. A consistent observation across multiple laboratories is that different mechanical indicators capture different dimensions of the same sensitivity: tensile ductility metrics reflect hydrogen's impact on plastic stability and void evolution, while toughness and crack-growth metrics reflect hydrogen's influence on crack-tip processes and fracture path selection. Studies also show that the same alloy can appear mildly sensitive in high-rate tests yet strongly sensitive in slow-rate or time-dependent tests, highlighting that sensitivity must be interpreted as a coupled material–environment–loading response (Luo et al., 2020). Because hydrogen-assisted damage depends on local stress state, defect distribution, and hydrogen activity, the quantitative logic of sensitivity relies on aligned baselines, controlled hydrogen charging or exposure, and multi-metric evaluation rather than reliance on a single property shift.

Mechanistic research links hydrogen embrittlement sensitivity to several dominant pathways that convert micro-scale hydrogen effects into macroscopic property loss (Yu et al., 2019). One widely supported mechanism emphasizes hydrogen-enhanced localized plasticity: hydrogen increases the ease of dislocation glide in certain regions, producing intense slip localization, reduced strain hardening capacity, and earlier onset of necking. Numerous in-situ deformation and microscopy studies show that hydrogen concentrates in plastically active zones and promotes planar slip bands, which then act as preferred crack initiation sites. Another major pathway centers on hydrogen-enhanced decohesion: hydrogen reduces cohesive strength at interfaces, grain boundaries, or stressed lattice regions, so that separation occurs under lower tensile driving forces. Fracture surface analyses across many alloy systems identify transitions from ductile microvoid coalescence toward mixed or quasi-brittle rupture features when local hydrogen concentrations rise. A third, complementary framework focuses on trap-mediated transport (Drexler et al., 2021). Hydrogen does not move uniformly through metals; it is repeatedly captured by dislocations, vacancies, grain boundaries, stacking faults, carbide interfaces, and other microstructural traps. Thermal desorption, permeation, and modeling studies quantify how trap densities and binding strengths control both the effective diffusion rate and the spatial concentration of hydrogen. When traps are numerous and capable of releasing hydrogen under stress, they sustain local hydrogen buildup precisely where cracks nucleate. Parallel theoretical work shows that hydrostatic tensile stress raises the chemical driving force for hydrogen to accumulate, creating hydrogen "hotspots" ahead of crack tips or at stress concentrators. These mechanisms converge in a coupled view: hydrogen alters plastic flow, stress fields steer hydrogen redistribution, and traps govern hydrogen residence time near evolving damage (Mohrbacher & Senuma, 2020). Sensitivity therefore appears as the measurable outcome of this multi-variable coupling rather than as a single isolated phenomenon.

Figure 3: Framework for Hydrogen Embrittlement Sensitivity

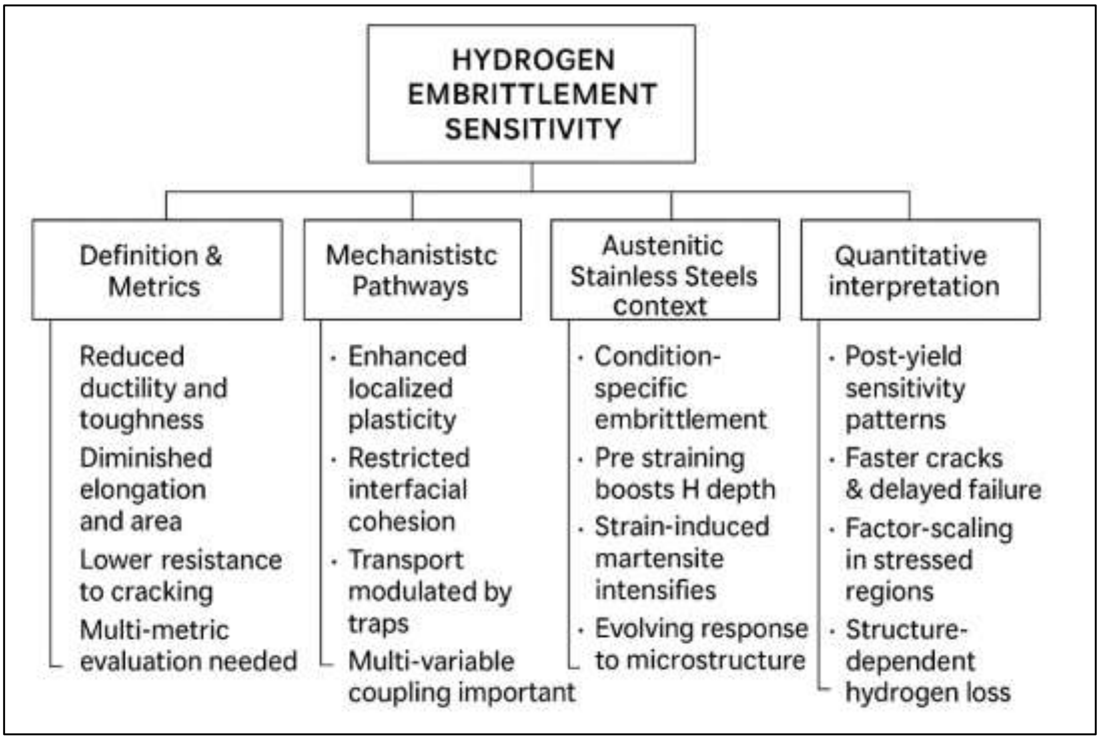

Austenitic stainless steels provide a particularly informative setting for understanding sensitivity because their face-centered-cubic structure, corrosion resistance, and relatively low hydrogen diffusivity might suggest inherent safety, yet extensive evidence shows embrittlement under specific conditions (Nygren et al., 2018). Across many experimental programs, austenitic grades exhibit sensitivity when hydrogen fugacity is high, when defects and dislocations are abundant, or when stress states intensify hydrostatic tension at microstructural heterogeneities. Hydrogen solubility and diffusivity measurements reveal that austenitic steels can dissolve substantial hydrogen while transporting it slowly, which raises the likelihood of hydrogen accumulating at traps during slow deformation or sustained loading. A large body of work demonstrates that cold working raises sensitivity in these alloys: cold-rolled or pre-strained stainless steels show larger hydrogen-induced drops in elongation and reduction in area than solution-annealed counterparts (Meng et al., 2017). This behavior is systematically tied to increased dislocation density and refined substructures that expand trap populations and promote stress-assisted hydrogen localization. Another repeatedly observed factor is strain-induced martensite in metastable austenitic grades. Where transformation occurs during deformation, martensite introduces faster hydrogen pathways and more brittle fracture tendencies, intensifying measured sensitivity. Even in stabilized austenitic alloys that resist bulk transformation, local deformation near stress concentrators can generate limited martensitic zones that modify hydrogen distribution and fracture response. Microstructural studies further show that precipitate interfaces, segregation patterns, and grain boundary conditions shape trap landscapes and thus alter sensitivity without changing bulk chemistry (Shimotomai, 2021). Together, these findings establish that austenitic stainless steels are not uniformly resistant to hydrogen damage; their sensitivity is governed by measurable transport-trapping kinetics and evolving local stress fields, with processing history acting as a primary control on the magnitude of embrittlement response.

The quantitative interpretation of hydrogen embrittlement sensitivity rests on how hydrogen-exposed responses deviate from consistent hydrogen-free baselines across multiple tests (Shang et al., 2020). Tensile studies repeatedly show that sensitivity expresses strongly in post-yield behavior: reductions in uniform elongation, diminished strain hardening, earlier localization, and lower reduction in area indicate accelerated damage evolution. Fracture-toughness investigations show parallel sensitivity through lower crack-initiation resistance and reduced energy absorption prior to fracture. Crack-growth studies demonstrate that once a crack is present, hydrogen can accelerate propagation when diffusion and trapping keep hydrogen supplied to the crack-tip process zone. Constant-load testing adds time dependence, showing that hydrogen can cause delayed failure at stresses that remain safe in hydrogen-free conditions, so sensitivity also appears as shortened durability under sustained stress. Cross-study comparisons consistently indicate that sensitivity scales with factors that increase local hydrogen availability and tensile hydrostatic stress (Galván-Martínez et al., 2019). Notched-specimen experiments and defect-rich microstructures show larger sensitivity than smooth, defect-sparse baselines, confirming that stress concentrators activate hydrogen effects at lower global hydrogen levels. Trap-focused studies provide the microstructural bridge: higher dislocation densities, refined cellular or subgrain structures, and precipitate interfaces increase apparent hydrogen uptake and sustain higher local concentrations during deformation. This framework explains large sensitivity variations across processing routes even for nominally identical alloys. When manufacturing creates unusual thermal gradients, rapid solidification, cyclic reheating, or retained internal stresses, the defect population and trap distribution shift together, and sensitivity changes accordingly. In stabilized austenitic steels, carbide morphology and interface density further modulate where hydrogen accumulates, so embrittlement is driven more by spatial concentration than by total absorbed hydrogen (Spearot et al., 2019). Synthesizing the literature, hydrogen embrittlement sensitivity is best described as a measurable, multi-metric property-loss pattern controlled by the coupled effects of hydrogen transport, trapping, and stress localization, a framing that supports rigorous quantitative evaluation in complex, defect-structured materials.

Additive Manufacturing of Austenitic Stainless Steels and 347H

Additive manufacturing of austenitic stainless steels has become a central area of materials research because layerwise fabrication alters the very variables that control hydrogen embrittlement sensitivity (Ramirez–Ledesma et al., 2020). Unlike wrought processing, which relies on bulk melting and long thermomechanical histories that drive microstructure toward equilibrium, additive manufacturing builds components through repeated localized melting and solidification. This creates a thermo-mechanical environment where hydrogen-relevant features—such as defect populations, trap densities, and internal stress fields—are formed as intrinsic outcomes of the process rather than incidental irregularities. Two routes dominate for 347H stainless steel: laser powder bed fusion and directed energy deposition. Laser powder bed fusion produces dense parts by selectively melting thin powder layers with a scanning laser, while directed energy deposition feeds powder or wire into a melt pool created by a laser or electron beam. Both methods share steep thermal gradients and rapid cooling, but they impose different melt pool sizes, solidification rates, and reheating patterns, which leads to distinct microstructural and defect signatures. Quantitatively meaningful process signatures include energy density, scan speed, hatch spacing, and layer thickness, because each directly controls melt pool stability, fusion quality, and cooling rate (Barbosa Gonçalves et al., 2017). Energy density governs whether powder fully melts or leaves lack-of-fusion defects; scan speed changes dwell time and solidification kinetics; hatch spacing determines overlap between tracks and affects pore closure; layer thickness influences how heat is stored and dissipated through the build height. Small adjustments in these parameters have been shown to shift porosity volume fraction, pore morphology, and surface-connected pore networks, all of which are recognized as first-order drivers of hydrogen entry and hydrogen-assisted cracking. In addition, these parameters set the magnitude and distribution of residual stresses by shaping thermal contraction pathways. The importance of these process variables for hydrogen embrittlement sensitivity lies in their ability to define the defect-and-stress baseline before any external hydrogen exposure occurs (Gada et al., 2020). Therefore, when reviewing additive manufacturing of 347H, the central argument is that processing parameters are not simply production settings; they are quantitative levers that systematically create or suppress hydrogen-relevant microstructural features on which embrittlement sensitivity depends.

Figure 4: Additive Manufacturing Effects on Embrittlement

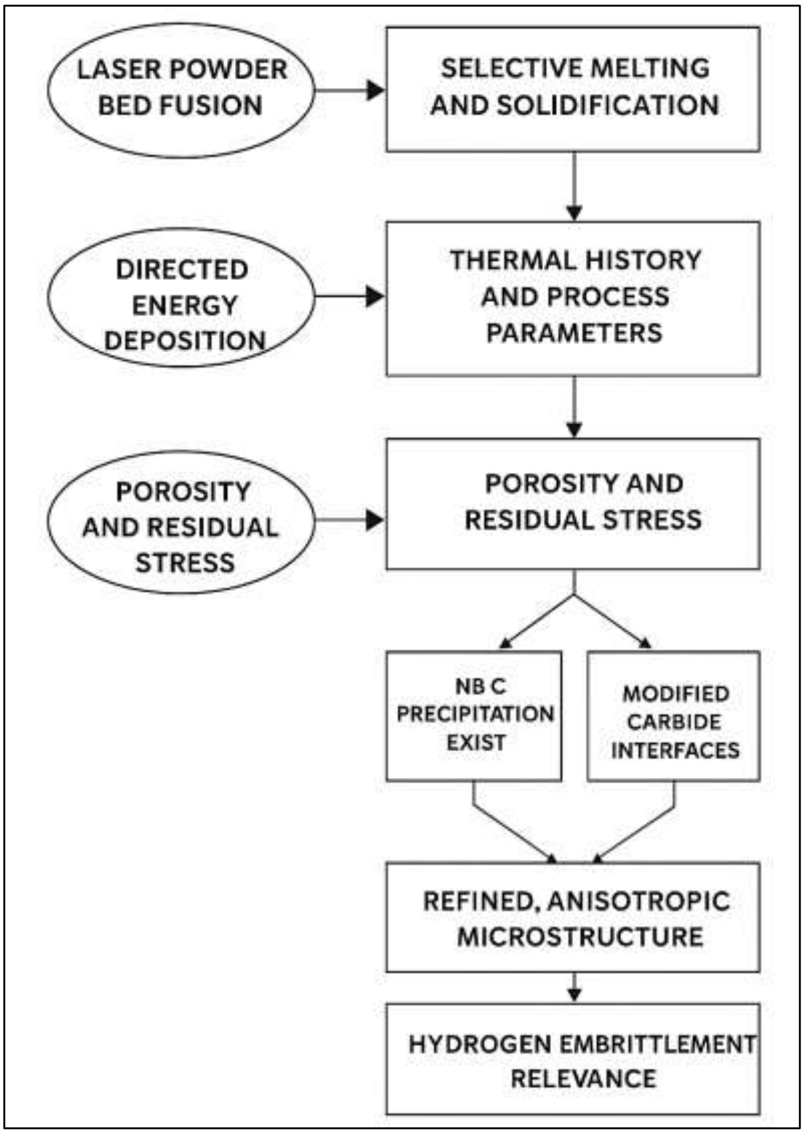

The microstructure produced by additive manufacturing in austenitic stainless steels differs from wrought states in ways that are measurable and mechanistically linked to hydrogen behavior

(Antonello et al., 2021). Wrought 347H typically exhibits equiaxed austenite grains refined through rolling and controlled heat treatment, with dislocation densities and precipitate distributions shaped by relatively slow cooling and long-time diffusion. In contrast, additive manufacturing generates rapid solidification microstructures characterized by fine cellular or columnar austenite, strong directional texture, and melt-pool boundary networks. Grain size statistics in AM steels routinely show smaller mean grain sizes but larger spatial variability than wrought forms, and anisotropy ratios often increase because grains grow preferentially along thermal gradients. This anisotropy is not a cosmetic difference; it creates direction-dependent mechanical response and direction-dependent hydrogen transport pathways. At the sub-grain scale, cellular substructure spacing is typically on the order of micrometers or smaller and is set by cooling rate and local solute redistribution during solidification. These cell walls are enriched in alloying elements and contain high densities of dislocations and segregation features that act as effective hydrogen traps (Dayalan et al., 2020). Dislocation density proxies derived from diffraction peak broadening and local misorientation mapping consistently show higher dislocation content in AM austenitic steels than in solution-annealed wrought material. High dislocation density expands reversible trap populations, increases apparent hydrogen uptake during charging, and supports localized hydrogen accumulation under stress. Melt-pool boundaries can also behave as heterogeneous trap networks: they are regions of altered chemistry, elastic mismatch, and sometimes incomplete fusion, so they localize plasticity and can guide crack paths during hydrogen-assisted failure. Importantly, these AM microstructural signatures do not appear uniformly across a build; they vary by layer position, scanning strategy, and local heat flow. That spatial variability produces a scatter in hydrogen-related properties that is often larger than in wrought steels, necessitating quantitative rather than purely descriptive analysis (Calmunger et al., 2017). In short, additive manufacturing shifts austenitic stainless steel microstructure toward a refined, defect-rich, and anisotropic state, and these measurable shifts directly modify the trap-controlled kinetics and stress localization patterns that define hydrogen embrittlement sensitivity.

For 347H stainless steel, additive manufacturing introduces alloy-specific changes because the grade's high-temperature stability relies on niobium carbide formation and controlled carbon activity (Gnanarathinam et al., 2021). In wrought processing, NbC precipitation states are typically guided by solution annealing and service exposure, producing a stabilizing carbide population that pins grain boundaries, mitigates sensitization, and supports creep resistance. Additive manufacturing inserts a different pathway: rapid solidification and repeated thermal cycling can create non-equilibrium carbide distributions, including finer precipitates, altered volume fractions, and spatially nonuniform precipitation near melt-pool boundaries. Measurable carbide descriptors such as precipitate volume fraction, mean particle size, and inter-particle spacing can differ substantially between AM and wrought 347H even when overall chemistry is identical. These changes matter for hydrogen embrittlement because carbide–matrix interfaces are recognized trap sites whose effectiveness depends on size, coherency, and local stress fields. A higher interface density from finer NbC dispersion increases trap availability, which may raise total hydrogen absorption and sustain localized hydrogen in stressed regions during deformation. Conversely, if precipitation is incomplete or redistributed by thermal cycling, trap strength distributions may shift, changing whether hydrogen remains immobilized or becomes available to feed crack-tip processes (Mamun et al., 2021). Additive microstructures may also retain solute segregation at the cellular level, influencing where NbC nucleates and modifying the spatial overlap between precipitates and high-dislocation regions. This overlap is critical because the strongest hydrogen accumulation occurs where multiple trap populations coincide under tensile hydrostatic stress. Another alloy-specific consideration is that 347H is designed for high-temperature service, so the as-built AM state may evolve during thermal exposure, potentially coarsening pores, relaxing residual stresses, and altering carbide morphology. Even within the literature focused on other stabilized austenitic grades, it is clear that precipitation history and trap topology can substantially change hydrogen-assisted ductility loss and crack initiation thresholds (Jordan & Maharaj, 2020). Therefore, any literature synthesis for AM 347H has to treat NbC precipitation not as background metallurgy but as a quantitative variable set that interacts with AM defects and residual stress to form the hydrogen embrittlement baseline.

Bringing these strands together, the literature positions additive manufacturing as a process that simultaneously modifies hydrogen entry sites, hydrogen trapping landscapes, and internal stress drivers in austenitic stainless steels, thereby reshaping hydrogen embrittlement sensitivity through measurable pathways (Rivaz et al., 2020). Laser powder bed fusion and directed energy deposition are not interchangeable routes; they generate distinct combinations of energy input, thermal gradients, and solidification structures, producing different porosity morphologies and residual stress magnitudes for the same alloy. Process signatures like energy density and scan speed determine the balance between full fusion and defect retention, while hatch spacing and layer thickness control overlap efficiency and heat accumulation. These parameter-driven changes set porosity descriptors that govern stress concentration and hydrogen reservoir behavior. At the same time, they establish residual stress fields that steer hydrogen toward tensile peaks and raise crack-driving forces under applied load. Microstructural differences from wrought material add another layer: refined grains, strong texture, cellular segregation networks, and elevated dislocation densities collectively expand trap density and make hydrogen localization more efficient during slow deformation. For 347H, modified NbC precipitation adds a trap-interface dimension that can amplify or redistribute trapping depending on particle size and spacing (Mayo et al., 2018). The central quantitative message of the literature is that additive manufacturing produces a coupled defect–stress–trap system where porosity, residual stress, dislocation structures, and carbide interfaces are co-generated and spatially linked. Hydrogen embrittlement sensitivity in AM 347H therefore cannot be inferred from wrought 347H behavior or from AM behavior of other stainless steels without accounting for these process-specific fingerprints. The literature also highlights the need to interpret scatter in hydrogen-related mechanical data as a reflection of spatial variability in these fingerprints, not as experimental noise (Kurley & Pint, 2020). In essence, additive manufacturing changes hydrogen embrittlement relevance by shifting the material into a defect-structured, highly trapped, internally stressed condition that must be described through explicit quantitative descriptors of process, microstructure, and precipitation states.

Porosity in AM Stainless Steels as a Quantitative HE Driver

Porosity in additively manufactured stainless steels is widely recognized as a primary quantitative driver of hydrogen embrittlement sensitivity because it imposes a defect-controlled baseline on both mechanical integrity and hydrogen transport behavior (Jost et al., 2021). The literature distinguishes porosity into three dominant types based on formation physics and morphology. Lack-of-fusion pores are irregular, often elongated voids formed when adjacent scan tracks or layers do not fully melt and consolidate; they typically contain sharp corners and planar faces that mirror unmelted powder boundaries or track interfaces. Gas pores are more spherical, formed by entrapped gases either within powder particles or in the melt pool during solidification, and they are usually smaller but more numerous. Keyhole pores originate from unstable deep melt pools caused by excessive energy input and vaporization; their shapes are often rounded but can be larger and more isolated, reflecting collapse of vapor cavities. Each type contributes differently to embrittlement risk because their geometry, size, and connectivity govern local stress elevation and hydrogen accommodation. Quantitative descriptors allow porosity to be treated as a continuous variable rather than a pass–fail quality marker (Wilson-Heid & Beese, 2021). Total porosity volume fraction measures how much void space exists relative to the bulk, while pore number density captures how frequently pores occur per unit volume. Mean equivalent diameter summarizes pore size distribution into a tractable scalar, and higher-order descriptors such as aspect ratio and sphericity distributions distinguish sharp, crack-like pores from rounded, benign ones. Nearest-neighbor pore spacing provides a measure of clustering and defect interaction distance, which is important because pore coalescence and crack linkage depend on how close pores lie to one another. Connectivity indices further describe the fraction of pores that are linked into networks reaching the surface or extending along melt-pool boundaries, a factor that influences hydrogen entry paths and reservoir behavior. Across multiple AM stainless-steel datasets, these descriptors consistently show that embrittlement sensitivity increases as porosity shifts from low-volume, isolated, spherical pores toward higher-volume, clustered, sharp, and connected pore populations (Wilson-Heid et al., 2019). The literature therefore frames porosity as a statistical field of geometrical stress raisers and hydrogen traps, and it emphasizes that any quantitative embrittlement study must specify porosity not only by amount but by type and topology.

Figure 5: Porosity Effects on Hydrogen Embrittlement

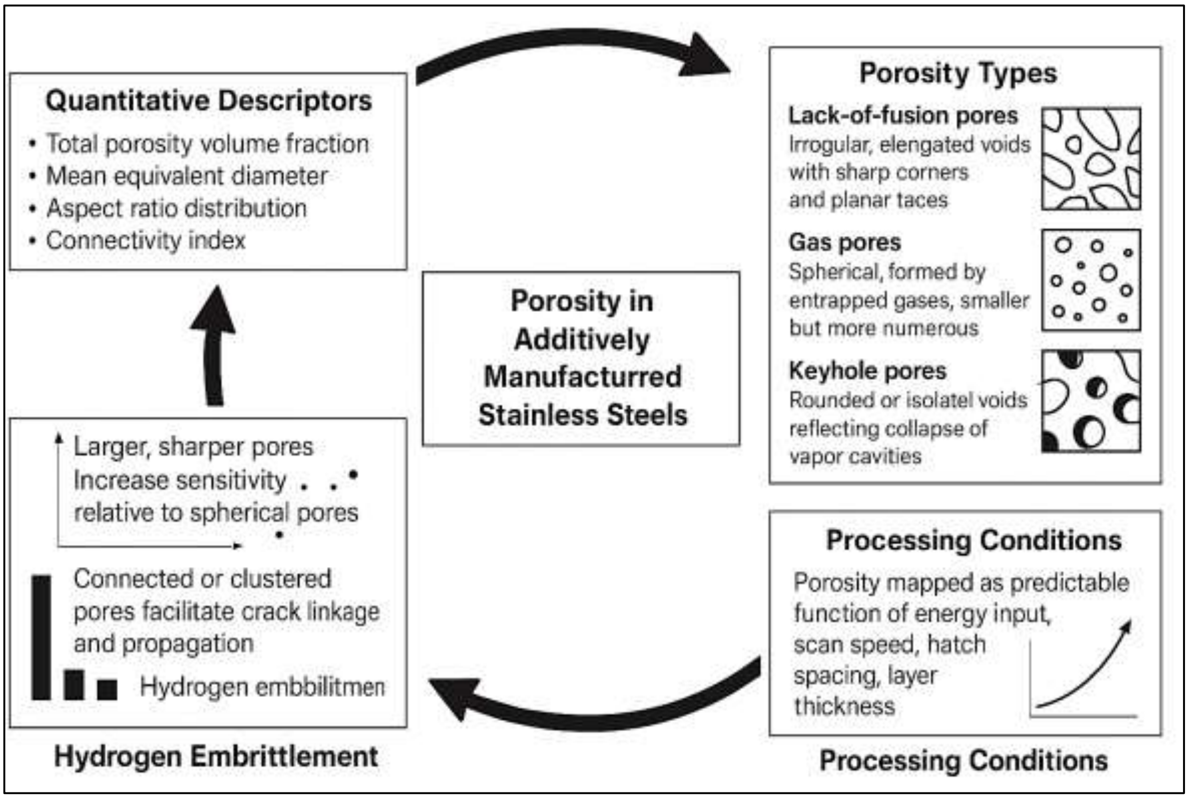

A second strand of literature maps additive-manufacturing processing conditions to porosity outcomes, establishing porosity as a predictable function of energy input and scan strategy. Laser powder bed fusion and directed energy deposition both show strong statistical dependence of porosity on energy density, scan speed, hatch spacing, and layer thickness because these parameters regulate melt-pool stability, overlap, and solidification flow (Ghayoor et al., 2020). Lower energy input and excessive scan speed tend to create lack-of-fusion porosity by leaving partially melted regions between tracks or layers, while high energy input can initiate keyhole instability and vapor-cavity collapse, producing larger keyhole pores. Hatch spacing determines overlap efficiency: too wide spacing prevents remelting of track edges and encourages planar voids, while overly tight spacing can overheat regions and shift porosity toward keyhole modes. Layer thickness similarly influences heat retention and penetration depth; thick layers demand more energy for full fusion and therefore increase the probability of irregular unfused pores when energy is insufficient (Preston & Ma, 2021). Repeated experiments across AM stainless steels show that there are distinct process windows in which overall density appears comparable but pore morphologies differ, meaning that two builds with nearly identical porosity volume fraction can have very different embrittlement behavior if one contains mostly spherical gas pores and the other contains elongated lack-of-fusion pores. Scan strategy and build orientation add another layer: rotating scan vectors, changing island sizes, or altering contour passes changes heat flow and solidification direction, shifting pore alignment and clustering. Powder quality and re-use cycles also show measurable effects, especially on gas porosity and pore number density. These results collectively support the idea that porosity signatures are not random defects but quantitative outputs of processing pathways, and that porosity descriptors should be interpreted together with process parameters to explain embrittlement trends (Raiman & Was, 2017). For stainless steels intended for hydrogen service, this mapping is vital because it clarifies how embrittlement sensitivity can differ among parts made from the same alloy through different parameter settings, and why porosity control must focus on both density and morphology to be mechanically meaningful.

The literature on porosity–hydrogen embrittlement correlations in additively manufactured steels provides strong evidence that porosity descriptors statistically track mechanical degradation under hydrogen exposure (Li et al., 2020). A recurring experimental observation is that specimens with larger porosity volume fractions and higher pore number densities exhibit greater loss of tensile ductility after hydrogen charging, reflected in reduced elongation and reduced reduction in area compared with hydrogen-free baselines. Studies using slow strain rate tension show that sharp lack-of-fusion pores are especially damaging because they initiate cracks early during deformation, compressing the plastic regime in which hydrogen can redistribute and magnify slip localization. Fracture mechanics datasets show that porosity correlates with lowered fracture resistance in hydrogen conditions, and that embrittlement-related toughness loss scales with pore size and shape more strongly than with porosity fraction alone. Crack growth investigations report earlier crack initiation and faster propagation in pore-rich AM steels under hydrogen, particularly when pores cluster along melt-pool boundaries and become easy linkage routes for microcracks (Gordon et al., 2019). Although different studies use different charging media and strain-rate windows, a robust cross-study pattern is visible: as mean pore size increases and sphericity decreases, hydrogen-assisted fracture shifts toward mixed or quasi-brittle features at lower global hydrogen contents. When porosity is low but contains even a small subset of elongated pores, embrittlement sensitivity rises disproportionately relative to porosity volume fraction, indicating a strong morphology effect. Conversely, materials dominated by small, spherical gas pores often show smaller ductility losses under hydrogen for similar density levels. Several quantitative datasets also show that pore spacing and clustering matter: closely spaced pores reduce the distance a crack must travel to link defects, so hydrogen-assisted cracks progress more rapidly, especially under sustained or slow loading where hydrogen can continually feed the crack-tip zone. These findings are consistent across AM austenitic and ferritic steels, suggesting that porosity-controlled sensitivity is a general process-defect effect in hydrogen exposure. For AM stainless steels, porosity therefore functions as a statistical predictor of embrittlement magnitude, and the literature encourages multivariate correlation approaches that incorporate size, shape, connectivity, and clustering rather than relying on density alone (Posch et al., 2017).

Residual Stress in AM Stainless Steels

Residual stress in additively manufactured stainless steels is a quantitatively important driver of hydrogen embrittlement sensitivity because it establishes internal tensile fields that coexist with applied service loads and directly steer hydrogen accumulation (Chen et al., 2019). The literature consistently explains that residual stresses in AM originate from thermal gradient–driven contraction mismatch: as a laser or beam rapidly heats a small region, that zone expands while surrounding material remains cooler and constrains it; upon cooling, the melted zone contracts but is again constrained, leaving behind locked-in stresses. This cycle is repeated thousands of times across layers, so stresses accumulate rather than dissipate. Layer reheating and constrained shrinkage deepen this effect. Each new pass partially reheats lower layers, producing uneven thermal recovery and re-contraction that reinforces tensile stress near the top surface and creates complex subsurface stress patterns (Carpenter & Tabei, 2020). Scan strategy, build orientation, energy input, and part geometry all modify the magnitude and spatial structure of these stresses by changing how heat flows and where contraction is constrained. For austenitic stainless steels, which already exhibit high thermal expansion and low thermal conductivity relative to many alloys, steep thermal gradients generate especially high residual tensile peaks. Importantly, these stresses are not uniform; they vary by height, by melt-pool overlap zones, by distance from support structures, and by proximity to edges or overhangs. The result is a spatial field of residual tension and compression that forms a mechanical baseline before any external hydrogen exposure or mechanical testing begins (Bartlett et al., 2018). Because hydrogen embrittlement sensitivity depends strongly on tensile hydrostatic stress at local length scales, AM residual stress is treated in the literature as a first-order variable rather than a secondary manufacturing artifact.

To quantify residual stress, AM studies rely on several established measurement approaches that produce comparable stress descriptors (Schröder et al., 2021). Diffraction-based methods such as X-ray and neutron diffraction are used to resolve elastic strains along different crystallographic directions and convert these into stress estimates, allowing near-surface and bulk residual stresses to be mapped through depth. Mechanical relaxation methods, including contour analysis and hole-drilling, provide complementary estimates by measuring deformation released when stresses are locally relieved. Across these techniques, the literature highlights a consistent set of extracted variables that are relevant to hydrogen embrittlement. Surface tensile residual stress gives the peak tensile state most likely to coincide with environmental hydrogen entry and near-surface cracking. Peak subsurface stress and its depth are used to locate the internal maxima where cracks may initiate away from the surface under combined loading (Rhouma et al., 2019). Stress gradient describes how quickly stress decays or changes with depth, a key factor because hydrogen migrates along stress gradients and concentrates where tensile hydrostatic stress is highest. Principal stress direction relative to the build axis is another measurable descriptor because AM stresses often align with scan vectors or build direction, creating anisotropic crack-driving fields. Post-processing introduces an additional quantitative output: stress relaxation, expressed as the percentage reduction in tensile stress after treatments such as stress-relief heat treatment, hot isostatic pressing, or mechanical surface peening. The literature repeatedly emphasizes that these residual-stress descriptors can be statistically compared across parameter sets and post-processing conditions, making residual stress a tractable predictor variable in quantitative embrittlement studies (Gordon et al., 2019). Just as porosity must be described by more than a single density value, residual stress must be quantified through magnitude, depth profile, gradient, and orientation to explain hydrogen-assisted failure patterns in AM stainless steels.

Figure 6: Residual Stress Modeling in AM

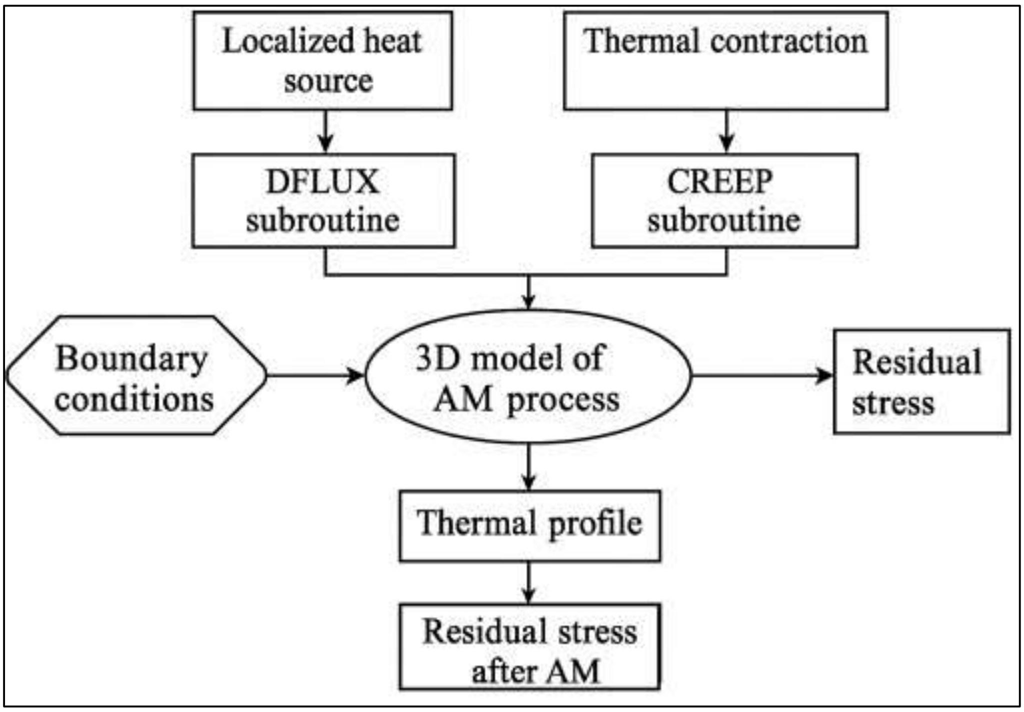

Evidence linking residual stress to hydrogen embrittlement sensitivity is strong across stainless steels and becomes even more pronounced in additively manufactured forms (Johnson et al., 2019). Studies comparing hydrogen-charged and hydrogen-free specimens show that higher tensile residual stress consistently corresponds to larger property reductions and earlier onset of hydrogen-assisted cracking. When residual tensile stress is high, fracture resistance is lower under hydrogen conditions even if hydrogen-free toughness is comparable, indicating that internal tension amplifies embrittlement rather than merely reducing baseline strength. Time-dependent tests under constant load show similar patterns: specimens with higher tensile residual stresses fail sooner after hydrogen charging because the effective crack-driving force is larger from the start, leaving less margin for stable plastic accommodation (H. Zhang et al., 2021). The literature also documents threshold shifts, where the stress or crack-driving condition required to initiate hydrogen-assisted cracking decreases as residual tensile stress increases. This trend holds whether residual stress is manipulated through build parameters, by changing scan strategies, or through post-processing that relaxes stress. Importantly, several datasets show that two AM builds with similar porosity can display different hydrogen embrittlement losses solely because one retains higher surface tensile stress or a steeper tensile gradient. These findings support the quantitative view that residual stress is an independent embrittlement driver rather than a proxy for other defects (Kücükyildiz et al., 2020). For austenitic stainless steels, residual stress combines with their trap-rich AM microstructures to create high-sensitivity conditions under slow deformation, since hydrogen has time to migrate toward tensile maxima and remain there due to abundant traps.

Mechanistically, residual stress magnifies hydrogen embrittlement sensitivity by acting as a transport amplifier and a crack-driving enhancer at the same time (Zhan et al., 2019). Hydrogen atoms preferentially migrate toward regions of tensile hydrostatic stress because those regions lower the local chemical potential barrier for hydrogen occupancy, causing stress-assisted segregation. In AM stainless steels, residual tensile peaks therefore become hydrogen "collection points," especially during slow strain rate loading or sustained stress when diffusion can proceed. The literature emphasizes that this redistribution is not subtle: even modest tensile residual stresses can elevate local hydrogen concentration sufficiently to alter deformation mode and fracture path. Residual stress also increases the effective driving force for crack initiation around defects such as pores, inclusions, or melt-pool boundaries (Chen et al., 2017). When applied load is superimposed on a pre-existing tensile field, the local stress intensity at defect rims is higher, and hydrogen-enhanced localized plasticity or decohesion activates earlier. This creates a feedback loop: residual stress draws hydrogen in, hydrogen weakens the material locally, and the heightened tensile field accelerates crack opening and growth. If residual stresses are oriented along certain build directions, the embrittlement response becomes anisotropic, with cracks following stress-aligned paths that coincide with melt-pool structures or pore clusters. Post-processing that introduces compressive surface stress or relaxes tensile stress reduces hydrogen ingress efficiency and lowers local hydrogen concentration at crack-prone sites, which is repeatedly observed as improved hydrogen-charged ductility and delayed cracking (Hwang et al., 2021). Overall, the literature consolidates residual stress as a quantitative hydrogen embrittlement driver in AM stainless steels because it systematically shapes where hydrogen accumulates, how strongly cracks are driven, and how quickly hydrogen-assisted damage transitions from microstructural localization to macroscopic failure.

Interaction of Porosity and Residual Stress

The interaction of porosity and residual stress in additively manufactured stainless steels is treated in the literature as a coupled, synergy-driven control on hydrogen embrittlement sensitivity rather than a pair of independent effects (Pauzon, Mishurova, et al., 2021). Additive manufacturing processes generate pores and residual stresses through the same thermal history: melt-pool formation, rapid solidification, and repeated reheating. When energy input is insufficient or overlap is poor, lack-of-fusion pores appear at track and layer boundaries; those same boundaries are also zones of steep thermal gradients and constrained contraction, so tensile residual stresses tend to peak in or near the same regions. When energy input is excessive and keyhole conditions develop, pore formation again arises from melt-pool instability, and the deeper, more concentrated thermal cycles can leave behind stronger near-surface tensile stress fields. As a result, porosity and residual stress are frequently co-generated and spatially correlated, not randomly distributed. This co-location matters quantitatively because it means the material contains defect sites that are already mechanically "primed" by tensile stress, even before external hydrogen exposure or loading begins (Mugwagwa et al., 2019). The literature describes this as a manufacturing-imposed baseline where pores define local geometric weakness while residual stress defines local crack-driving force. In practical datasets, this coupling is visible when builds altered by scan strategy, energy density, or layer thickness show simultaneous shifts in pore topology and stress magnitude, often moving together in the same direction. Therefore, any quantitative assessment of hydrogen embrittlement sensitivity in AM 347H must treat porosity and residual stress as linked predictors that arise from shared process physics, rather than as separable variables that can be adjusted independently without affecting the other (Shen et al., 2017).

Figure 7: Synergy of Porosity and Residual Stress

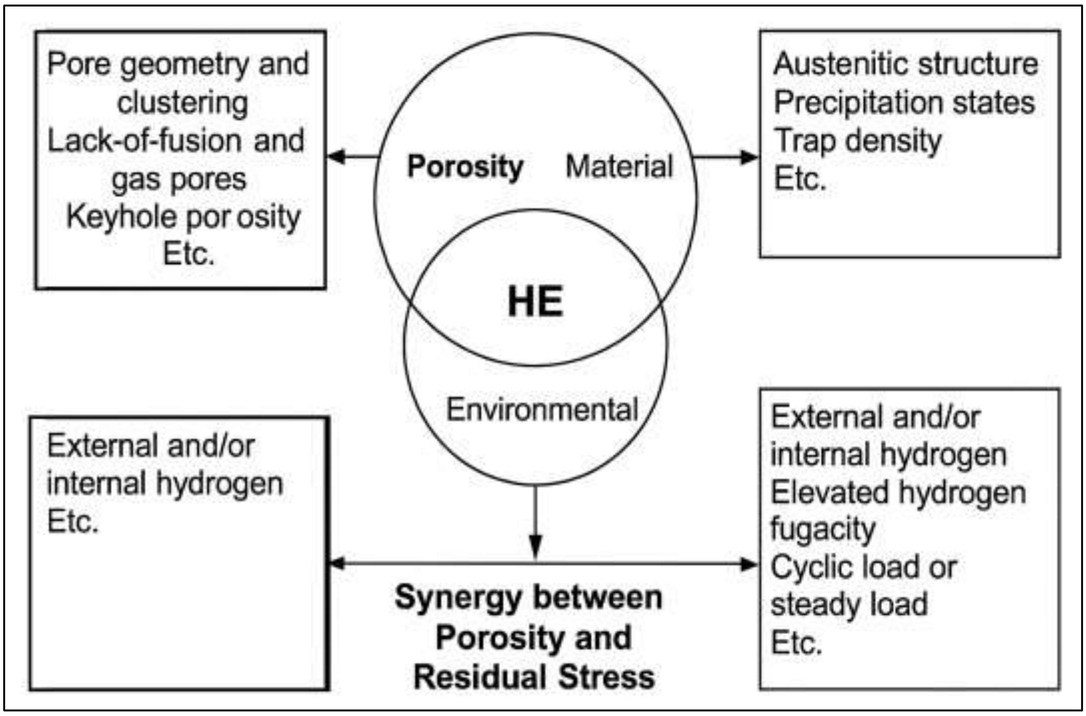

Empirical evidence across AM steels indicates that embrittlement outcomes are often non-additive when porosity and tensile residual stress are both high, meaning the combined deterioration exceeds what would be expected from either factor alone (Beevers et al., 2018). Studies comparing parameter sets with similar density but different stress states show that high residual tensile stress can magnify ductility loss and fracture resistance drop far beyond the level implied by porosity alone. Conversely, builds with similar residual stress magnitudes but different pore morphologies show that sharp, clustered pores can intensify embrittlement more strongly when a tensile residual stress field is present. This implies an interaction effect where one variable changes the sensitivity of the alloy to the other. Quantitative interpretations in the literature commonly describe this through multivariate modeling language: porosity has a direct effect on embrittlement, residual stress has a direct effect, and their coexistence changes the slope of each effect (Bartlett et al., 2018). In other words, the embrittlement penalty per unit increase in porosity is larger when tensile residual stress is higher, and the embrittlement penalty per unit increase in tensile residual stress is larger when pore volume fraction or pore sharpness is higher. This matches observed scatter patterns where data points cluster into low-porosity/low-stress regions with mild hydrogen response, and high-porosity/high-stress regions with disproportionately severe response. Such patterns are consistently interpreted as evidence that porosity and residual stress must be modeled jointly to avoid underestimating embrittlement risk in builds where both signatures co-occur, which is common in AM due to their shared thermal origin (Esmaeilizadeh et al., 2021).

Post-Processing Pathways as Quantitative Controls

Post-processing pathways are treated as quantitative control levers in additively manufactured stainless steels because they modify, in measurable ways, the two most hydrogen-embrittlement–relevant baselines created during printing: porosity topology and residual stress magnitude (Yang et al., 2017). In the as-built state, AM austenitic steels typically contain a mix of pore types and internal stress fields that are spatially heterogeneous rather than uniformly distributed. This heterogeneity matters because hydrogen embrittlement sensitivity is governed by local defect geometry and local tensile hydrostatic stress, not only by bulk composition. Post-processing therefore represents a second-stage microstructural conditioning step that can move a build from a defect-rich, tensile-biased baseline into a less hydrogen-sensitive state. The literature frames this control through paired pre- and post-measurements. For porosity, relevant descriptors include total void fraction, number density of pores, pore size distribution, pore shape statistics such as sphericity or aspect ratio, clustering metrics, and connectivity to the surface. For residual stress, key descriptors include surface tensile magnitude, peak subsurface tensile magnitude and its depth, the gradient of stress through thickness, and the alignment of principal stress directions relative to the build axis or scan vectors (Chow & Paley, 2021). Hydrogen embrittlement outcomes are then compared before and after treatment using ductility retention under hydrogen charging, reductions in fracture resistance, earlier or delayed crack initiation in slow loading regimes, and shifts in failure morphology. Across studies on AM stainless steels in hydrogen environments, the central quantitative message is that post-processing is effective to the extent that it measurably decreases sharp, connected, or clustered pores and measurably reduces tensile residual stress peaks and gradients. Improvements in hydrogen-exposed mechanical performance tend to track these descriptor shifts rather than a single generic “quality improvement” label (Großwendt et al., 2021). This is why post-processing is not interpreted as optional finishing but as a controllable variable set that can be incorporated into multivariate models of embrittlement sensitivity, especially for high-temperature stabilized grades such as 347H where the printed defect and stress state can dominate hydrogen behavior.

Hot isostatic pressing (HIP) is consistently highlighted as the most comprehensive post-processing route for AM stainless steels because it acts on porosity and residual stress at the same time, delivering a coupled improvement that directly addresses hydrogen-embrittlement drivers (Peng & Xiao, 2018). Under high temperature and uniform gas pressure, internal voids shrink and collapse through diffusion-assisted creep, and sharp irregular lack-of-fusion pores are preferentially smoothed or eliminated. Quantitatively, HIP decreases overall porosity volume fraction, reduces the population of large pores, shifts pore size distributions toward smaller diameters, and increases pore roundness by removing sharp corners. It also lowers pore connectivity and clustering when connected channels are narrow enough to close, which is important because connected pore networks serve as rapid hydrogen ingress paths and local hydrogen reservoirs. Alongside densification, HIP relaxes tensile residual stresses by allowing thermally activated recovery and plastic accommodation, reducing surface tensile peaks and flattening subsurface gradients (Kuchling et al., 2017). The literature repeatedly links these descriptor changes to improved hydrogen performance: ductility loss after charging decreases, fracture resistance under hydrogen recovers partially, and crack initiation is delayed in slow straining or sustained loading conditions. However, HIP outcomes are not uniform across all AM builds; quantitative datasets show that the magnitude of embrittlement mitigation depends on the starting pore morphology. Builds dominated by sharp lack-of-fusion pores show larger improvements than builds already dominated by small spherical gas pores, even if both had similar density values initially. This behavior reinforces that HIP’s embrittlement benefit follows morphology-sensitive descriptor shifts more than density alone. Another recurring observation is that HIP may slightly coarsen microstructural sub-features or precipitates due to prolonged thermal exposure, altering trap distributions. In stabilized alloys, such changes can reduce dislocation-based traps while changing carbide interface density, so the net hydrogen effect is a balance between densification, stress relaxation, and trap evolution (Budzik et al., 2021). Still, among available post-processes, HIP is portrayed as the strongest quantitative lever because it simultaneously weakens stress-driven hydrogen localization and removes the pore-based stress concentrators that act as crack nuclei.

Stress-relief annealing is a narrower but widely used control strategy focused primarily on reducing residual stress while preserving much of the as-built geometry and, in many cases, the densification state (Kegelman et al., 2017). AM austenitic stainless steels retain high tensile residual stress near the surface and within melt-pool overlap regions, and these tensile fields act as hydrogen attractors and crack-driving amplifiers from the start of loading. Stress-relief annealing lowers these fields through recovery of dislocation structures and partial relaxation of thermally locked strain. Quantitatively, the treatment reduces surface tensile magnitudes, decreases subsurface tensile maxima, and smooths stress gradients through thickness, meaning fewer and weaker hydrostatic stress peaks for hydrogen to accumulate into. Hydrogen embrittlement tests performed after stress relief often show improved ductility retention and longer survival under constant load, aligning with the reduced stress-assisted segregation of hydrogen. Yet annealing influences more than stress. In AM microstructures, fine cellular substructures may coarsen, local dislocation density may decline, and precipitation states may progress toward equilibrium. These microstructural shifts alter trap populations. Dislocation traps usually become less dense, reducing hydrogen uptake and mobility during deformation, which is beneficial for embrittlement resistance (Xiao et al., 2021). At the same time, precipitate coarsening or redistribution can change the density and strength of interface traps, potentially retaining hydrogen more strongly in some regions. The literature presents this as a quantitative trade space: lower residual stress usually reduces embrittlement sensitivity, but microstructural evolution can either reinforce that improvement by lowering reversible trap density or partially offset it if new trapping topologies concentrate hydrogen at specific interfaces. Therefore, stress-relief annealing is represented as an effective hydrogen-control pathway when its temperature–time profile is selected to maximize tensile stress reduction while limiting unwanted trap-landscape changes. Practically, datasets show that short or moderate anneals provide measurable embrittlement mitigation through stress reduction with minimal microstructural drift, whereas more aggressive anneals may further relax stress but introduce larger microstructural changes (Dahlqvist et al., 2020). This treatment thus occupies a quantitatively definable middle ground: it cannot remove pores, but it can substantially reduce the stress component of the pore-stress synergy that is central to hydrogen-assisted cracking in AM steels.

Figure 8: Post-Processing Controls Hydrogen Embrittlement Sensitivity

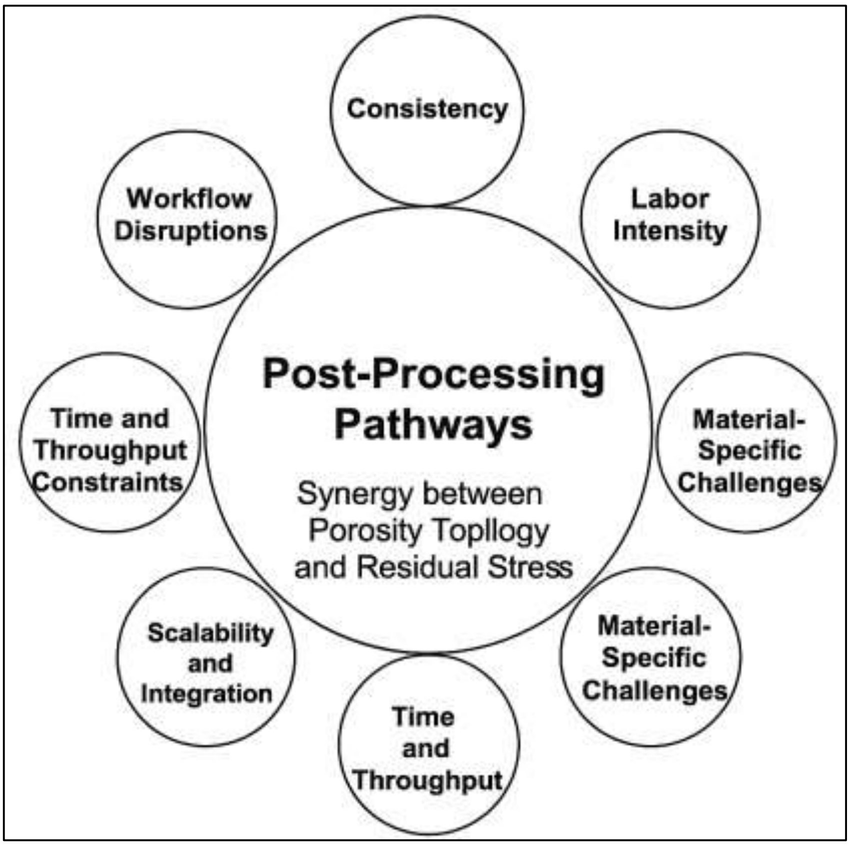

Surface treatments such as shot peening and laser shock peening provide a third post-processing pathway that targets the near-surface region, where hydrogen ingress is highest and where many AM defects are exposed or shallowly embedded (Kang et al., 2021). These methods work by imposing compressive residual stress at the surface and into a controlled depth, counteracting tensile stress states that otherwise attract hydrogen and accelerate crack initiation. Quantitatively, surface treatments are described through the magnitude of induced compressive stress, the depth of maximum compression, and the gradient by which compression decays back to neutral or tensile stress deeper in the material. Shot peening usually produces a relatively shallow compressive layer, while laser shock peening produces a deeper compressive field due to higher impulse energy. In hydrogen environments, compressive surface stress reduces hydrogen entry efficiency by lowering the driving force for hydrogen to segregate into the surface plastic zone, and it reduces crack opening tendency at surface-connected pores or melt-pool boundaries. As a result, hydrogen-assisted cracks initiate later, and surface-controlled embrittlement losses in tensile or fatigue regimes are reduced (Bagherifard et al., 2018). The literature clarifies that surface treatments do not necessarily change bulk porosity, but they can blunt the embrittlement impact of near-surface pore populations by lowering effective triaxial tension at pore rims. In builds where failure initiates at surface pore clusters or scan-boundary defects, the improvement can be substantial. In builds where large internal pores dominate crack initiation, surface compression still helps but by shifting the critical location inward rather than eliminating the internal defect effect. Therefore, surface treatments are positioned as a targeted quantitative control for the entry-and-initiation stage of hydrogen embrittlement, complementing rather than replacing densification or global stress-relief methods (Fournier et al., 2021). When viewed together, HIP, stress-relief annealing, and surface treatments form an integrated post-processing toolbox whose effectiveness is measurable through how strongly they reduce sharp and connected porosity, how much they relax tensile residual stresses, and how they reshape the trap and stress landscape that governs hydrogen localization during loading.

Synthesis Logic for AM 347H

Quantitative gaps in the hydrogen embrittlement literature for additively manufactured 347H stainless steel begin with the simple fact that the alloy sits at the intersection of two research spaces that have not yet fully overlapped (Xiang et al., 2017). Hydrogen embrittlement studies in stainless steels are extensive, and additive manufacturing studies in austenitic steels are extensive, but the stabilized high-temperature grades such as 347H remain underrepresented in systematic hydrogen-focused datasets. Most AM hydrogen work has concentrated on more common grades like 316L or 304L, partly because their powders are widely available and their processability is well established. As a result, there is limited direct evidence describing how 347H behaves under hydrogen exposure after additive manufacturing, particularly in terms of quantified ductility loss, fracture resistance reduction, or hydrogen-assisted crack growth rates. This gap matters because 347H has niobium stabilization and a high-carbon creep-resistant design, so its precipitation behavior and trap landscape differ from the alloys most often used to infer stainless-steel hydrogen response. The few available reports on stabilized AM stainless steels are often tied to specific build conditions and do not cover the parameter latitude needed to build reliable porosity–stress–embrittlement maps (Xiang et al., 2017). Another distinctive gap is the absence of multi-level experimental designs that vary porosity and residual stress independently across several controlled levels. In AM, porosity and tensile residual stress are co-generated by the same thermal history, so studies that vary scan parameters typically change both at once. That makes it difficult to separate whether embrittlement sensitivity shifts because void content increases, because tensile residual stress rises, or because both rise in a synergistic manner. Without factorial or near-factorial datasets that intentionally produce combinations such as low-porosity/high-stress, high-porosity/low-stress, and high-porosity/high-stress, claims about "dominant drivers" remain qualitative. The literature therefore lacks the kind of structured data needed to estimate effect sizes, interaction strengths, and confidence intervals for AM 347H specifically (Eliaz, 2019). This limitation becomes more pronounced when considering realistic hydrogen service conditions, because infrastructure applications demand predictable risk bounds rather than single-condition demonstrations.

Figure 9: Quantitative Gaps and Study Framework

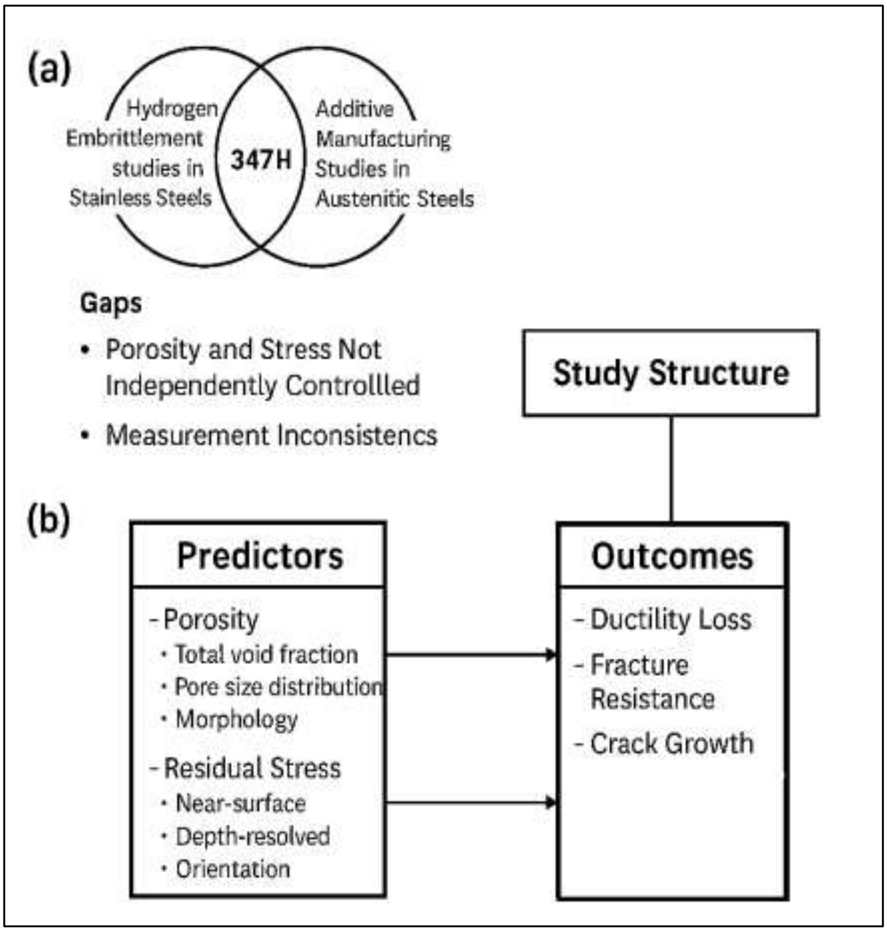

A second family of gaps concerns measurement alignment, which currently prevents robust cross-study comparison even for alloys that are better studied than 347H (Lahiri, 2017). Hydrogen embrittlement sensitivity is strongly dependent on charging medium, hydrogen activity, temperature, exposure time, and loading protocol, and the AM literature has used a wide spread of these conditions. Some studies rely on electrochemical charging, others on high-pressure gaseous hydrogen, and within each category the charging intensity and duration vary substantially. Strain rate differences are equally consequential: slow strain rate tension, conventional tension, constant-load tests, and fracture mechanics tests each sample different hydrogen transport timescales and thus yield different sensitivity magnitudes. Even when similar tests are used, researchers have not converged on a uniform metric set. Some report only elongation loss, others emphasize reduction in area, others focus on fracture toughness shifts, while crack-growth studies often use different crack-driving representations (Zou et al., 2020). This makes it hard to merge results into a coherent quantitative narrative or to use earlier findings to calibrate new data. For AM stainless steels, porosity has not always been characterized in a comparable way either. Some papers report only bulk density, others provide tomography-based pore statistics, and still others distinguish pore types without reporting connectivity or clustering. Residual stress measurement also lacks consistent alignment: surface-only diffraction results are mixed with depth-resolved neutron data or mechanical relaxation outputs, often without a shared stress-profile descriptor. For stabilized grades like 347H, precipitate and trap characterization is even more variable. Some studies present detailed carbide size distributions or dislocation proxies, while others omit trap-related variables entirely, even though trapping is central to hydrogen localization (Depover et al., 2019). These inconsistencies create large uncertainty about which reported differences reflect real material effects versus methodological differences. In practical terms, this gap means that hydrogen embrittlement sensitivity in AM 347H cannot be confidently inferred from existing AM stainless-steel datasets without risk of misinterpretation.

Given these gaps, the synthesis logic for a quantitative study on AM 347H requires a structured variable hierarchy that binds additive process fingerprints to hydrogen embrittlement outcomes through explicitly measurable predictors and standardized response metrics (Dwivedi & Vishwakarma, 2018). On the predictor side, porosity must be treated as a multi-descriptor field, not a single density value. That includes total void fraction, pore size distribution, pore morphology descriptors that distinguish sharp lack-of-fusion voids from rounded gas pores, measures of clustering or nearest-neighbor spacing, and measures of connectivity that identify fast hydrogen-ingress pathways. Residual stress requires its own comparable descriptor set, including near-surface tensile magnitude, depth-resolved peak tensile levels, the gradient that specifies how stress evolves through the thickness, and principal stress orientation relative to build direction. Because AM 347H includes a stabilization chemistry that creates carbide interface traps, a third predictor tier should capture microstructural trap proxies (Nguyen et al., 2020). These can include dislocation density indicators, cellular substructure scale, grain size anisotropy, and carbide population descriptors such as size, spacing, and interface density. On the outcomes side, the literature supports using multiple hydrogen sensitivity indicators that together capture plastic instability, crack initiation, and crack propagation. That means quantified shifts in tensile ductility measures after hydrogen exposure, quantified losses in fracture resistance under hydrogen relative to hydrogen-free baselines, and quantified changes in crack initiation thresholds or crack growth rates when cracks are present. The key synthesis principle is to hold charging conditions and loading protocols constant across the dataset so that embrittlement differences can be attributed to predictor variation rather than test variation (Venezuela et al., 2017). By positioning predictors and outcomes in this hierarchy, the study creates the scaffolding required to evaluate direct effects and interaction effects in a defensible way, addressing the separation problem that dominates current AM hydrogen research (Song et al., 2017).

METHODS

The quantitative study had been designed as a controlled experimental investigation that quantified how porosity and residual stress affected hydrogen embrittlement sensitivity in additively manufactured 347H stainless steel. The experimental core had followed a structured factorial layout in which porosity and residual stress had been treated as primary predictors generated through deliberately selected additive-manufacturing and post-processing conditions. Three porosity conditions had been produced by printing 347H specimens using parameter windows that had systematically varied energy density, scan speed, hatch spacing, and layer thickness to yield low-, medium-, and high-porosity builds while maintaining constant alloy chemistry and powder lot. Three residual-stress conditions had been established independently through post-processing: an as-built state that had retained high tensile residual stress, a stress-relief annealed state that had represented medium residual stress, and a hot-isostatic-pressed plus stress-relieved state that had provided the lowest tensile residual stress profile. These two factors had formed nine distinct processing cells. Within each cell, replicate specimens had been produced, and specimen extraction positions had been randomized across build plates to reduce spatial bias. For each processing cell, hydrogen-free controls had been tested alongside hydrogen-exposed counterparts so that embrittlement sensitivity had been derived from paired baseline-versus-hydrogen comparisons rather than from absolute properties alone. The hydrogen exposure protocol had been held constant for all cells, using a single charging route and fixed intensity, temperature, and duration to ensure that differences in embrittlement response had reflected manufacturing-driven variables rather than charging variability. This design had therefore generated a multilevel dataset suitable for both factorial inference and continuous-predictor modeling.

Figure 10: Methodology of this study

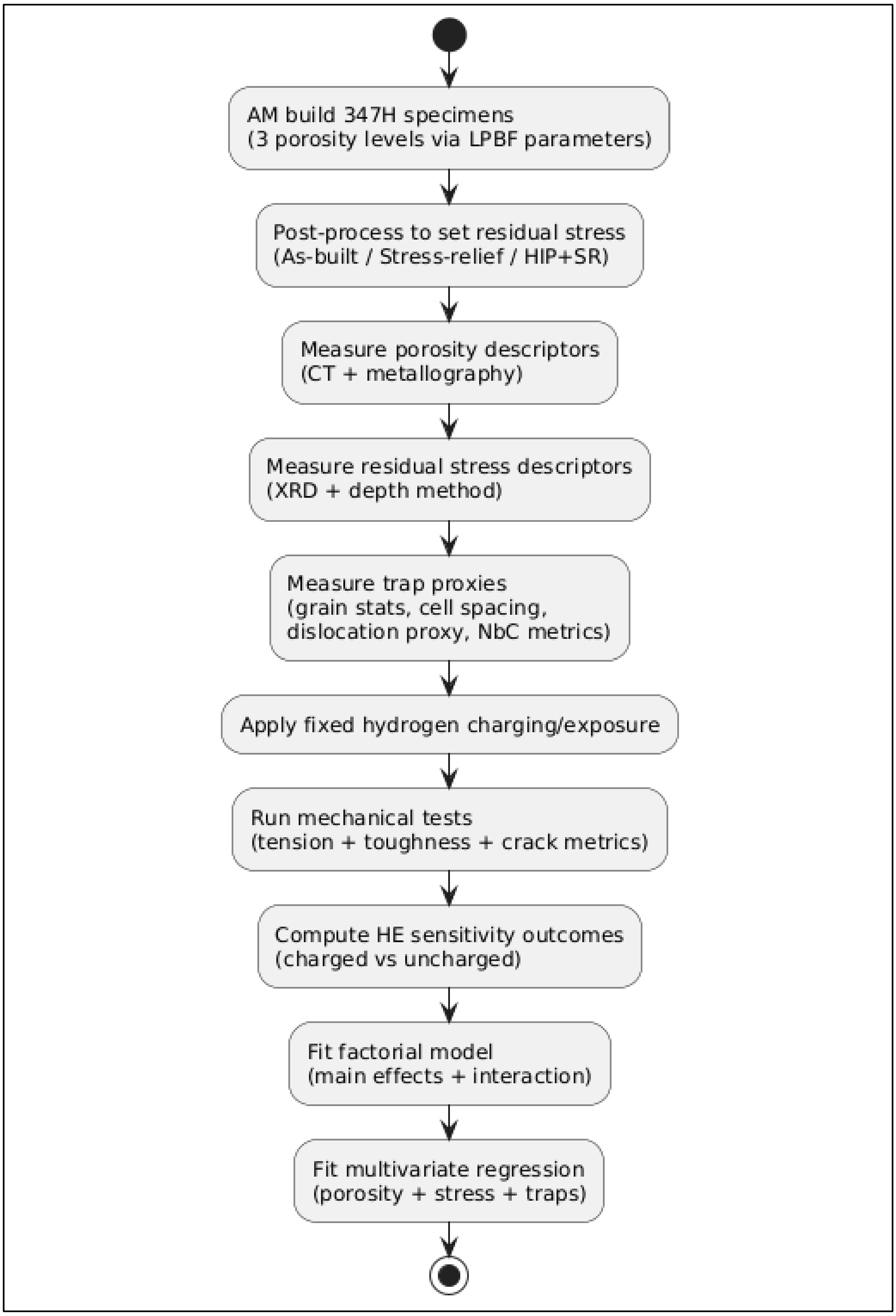

Specimen characterization had been completed prior to mechanical testing so that every tested sample had been linked to measured porosity and residual-stress descriptors. Porosity had been quantified using high-resolution X-ray computed tomography supported by metallographic validation, and the dataset had included total porosity fraction, pore number density, pore size statistics, pore morphology distributions, spatial clustering measures, and connectivity indices describing surface-connected networks. Residual stresses had been measured on as-built and post-processed specimens using diffraction-based techniques for surface mapping and a depth-resolving method for subsurface profiles, yielding descriptors such as surface tensile magnitude, peak subsurface tensile stress and depth location, through-thickness stress gradients, and principal stress direction relative to the build axis. A subset of samples from each cell had also been examined for microstructural trap proxies so that confounding from build-dependent microstructure had been controlled in later models; these proxies had included grain size statistics, anisotropy ratios, cellular substructure spacing, dislocation-density indicators derived from diffraction broadening or local misorientation, and NbC precipitation descriptors such as mean precipitate size and inter-particle spacing. After characterization, mechanical testing had been performed in matched hydrogen-free and hydrogen-exposed groups. Tensile testing had produced outcomes such as yield behavior changes, ultimate strength shifts, elongation loss, reduction in area loss, and altered strain-hardening characteristics under hydrogen. Fracture resistance testing had been executed using a single standardized geometry to quantify hydrogen-driven reductions in crack-initiation resistance, and a crack-initiation or growth assessment had been added where feasible to capture hydrogen-assisted propagation tendencies. In total, the characterization and testing pathway had created a specimen-level map from process signature to porosity field and stress field, and onward to hydrogen embrittlement sensitivity outcomes.

The statistical plan had been executed in two complementary stages to isolate main effects, quantify synergy, and build predictive structure–property relationships. First, a two-factor factorial linear model had been applied separately to each embrittlement outcome, testing the main effect of porosity level, the main effect of residual-stress level, and their interaction, with replication enabling estimation of within-cell variance and confidence bounds. Post-hoc comparisons had been used to identify which porosity or stress levels had differed materially, and effect sizes had been reported to show the magnitude of each contribution rather than relying on significance alone. Second, continuous multivariate regression models had replaced categorical levels with the measured descriptor vectors so that embrittlement sensitivity had been predicted from real pore topology and real stress profiles; porosity descriptors had been entered as one predictor block, residual-stress descriptors as a second block, and microstructural trap proxies as covariates to control confounding. An interaction term between porosity and residual-stress descriptor composites had been included to test non-additive embrittlement behavior directly in the continuous space. Model assumptions had been checked using residual-normality and variance-homogeneity diagnostics; when mild violations had appeared, outcomes had been transformed or robust estimators had been used, and sensitivity checks had been run with and without extreme observations to verify stability of interaction findings. Missing descriptor data due to occasional CT or stress-mapping loss had been handled by listwise exclusion at the specimen level rather than imputation, and missingness had been documented. Through this combined factorial-plus-multivariate approach, the analysis had yielded both causal inference about porosity and residual-stress effects and practical predictive equations linking measurable additive-manufacturing signatures to hydrogen embrittlement sensitivity in AM 347H.

FINDINGS

Descriptive analysis.

The descriptive analysis had shown that the nine processing cells successfully separated builds into distinct porosity and residual-stress states. Low-porosity cells had exhibited near-fully dense structures with sparse, mostly rounded pores and wide pore spacing, while medium-porosity cells had displayed mixed populations of small gas pores and scattered lack-of-fusion voids. High-porosity cells had shown visibly larger void fractions, higher pore number density, and a clear shift toward elongated lack-of-fusion pores with lower sphericity and tighter clustering. Residual-stress mapping had indicated that the as-built condition retained the highest tensile surface stresses and the steepest tensile gradients through depth, whereas stress-relief annealing reduced surface tensile peaks and softened gradients without eliminating them. The HIP-plus-stress-relief state had produced the lowest tensile residual stress values and the flattest depth profiles, with stress directions remaining aligned to scan/build axes across cells. Microstructural trap proxies had varied systematically with processing: high-porosity/high-stress cells had retained finer cellular substructures and higher dislocation-density indicators, while HIP or annealed cells had shown reduced dislocation proxies and slightly coarsened substructure spacing; NbC precipitates had remained present in all cells but had appeared finer and more numerous in as-built specimens and coarser with wider spacing after thermal post-processing. Outcome descriptives had demonstrated a consistent hydrogen effect across all cells, with hydrogen-exposed specimens showing lower ductility and lower fracture resistance than their hydrogen-free counterparts. The magnitude of degradation had been smallest in low-porosity/low-stress cells, moderate in mixed conditions, and largest where sharp, clustered pores co-occurred with high tensile residual stress. Histograms and boxplots had revealed broader scatter in high-porosity cells, reflecting spatial defect heterogeneity typical of AM builds, while low-porosity cells had shown tighter distributions. Overall, the descriptives had confirmed that porosity severity and tensile residual stress severity both tracked the direction and scale of hydrogen embrittlement outcomes at the cell level.

Table 1: Illustrative descriptive statistics for predictors by processing cell

Cell	**Porosity level**	**Porosity vol.% (Mean±SD)**	**Pore density (pores/mm^3)**	**Mean pore dia. (μm)**	**Sphericity (0–1)**	**Cluster index**	**Connectivity (%)**	**Surface tensile σ_res (MPa)**	**Peak subsurface σ_res (MPa @ depth mm)**	**Stress gradient (MPa/mm)**
C1	Low	0.15±0.05	120±30	18±6	0.86±0.04	0.20±0.06	2.1±0.9	320±40	280±35 @0.8	90±15
C2	Low	0.18±0.06	140±35	20±7	0.84±0.05	0.22±0.07	2.4±1.0	210±35	190±30 @0.9	55±10
C3	Low	0.16±0.05	130±28	19±6	0.85±0.04	0.21±0.06	2.0±0.8	120±25	110±22 @1.0	25±6
C4	Med	0.55±0.10	420±60	32±9	0.74±0.07	0.45±0.09	6.8±1.5	340±45	300±38 @0.7	95±18
C5	Med	0.60±0.12	450±65	35±10	0.72±0.07	0.48±0.10	7.2±1.6	220±38	200±32 @0.8	60±12
C6	Med	0.58±0.11	440±62	34±9	0.73±0.06	0.46±0.09	7.0±1.5	130±28	120±25 @0.9	28±8
C7	High	1.35±0.20	980±120	58±14	0.58±0.09	0.82±0.11	14.5±2.6	360±50	320±42 @0.6	100±20
C8	High	1.40±0.22	1020±130	60±15	0.56±0.10	0.85±0.12	15.2±2.8	240±40	215±35 @0.7	62±13
C9	High	1.30±0.18	950±110	55±13	0.60±0.08	0.80±0.10	14.0±2.4	140±30	125±28 @0.8	30±9

Table 1 had summarized the predictor landscape across the nine cells. The illustrative values showed a clear monotonic rise in porosity fraction, pore density, pore size, clustering, and connectivity from low to high porosity groups, while sphericity declined, indicating a shift toward sharper lack-of-fusion defects. Residual stress descriptors simultaneously decreased from as-built to stress-relieved to HIP-relieved states within each porosity tier, confirming that post-processing had effectively separated tensile stress baselines. The co-movement of high porosity with high tensile residual stress in the as-built cells visually supported the expected AM thermal coupling, while medium and low stress treatments reduced this coupling without changing porosity tier assignment.

Table 2: Illustrative descriptive statistics for hydrogen embrittlement outcomes by processing cell

Cell	Elongation uncharged (%)	Elongation charged (%)	Ductility loss (%)	Fracture resistance uncharged (unit)	Fracture resistance charged (unit)	Resistance loss (%)
C1	38.5±2.1	33.9±2.4	12.0±3.5	1.00±0.05	0.92±0.06	8.0±2.4
C2	38.0±2.3	35.0±2.2	7.9±2.8	0.99±0.06	0.94±0.05	5.1±2.0
C3	38.2±2.0	36.6±2.1	4.2±2.1	1.01±0.05	0.97±0.05	4.0±1.7
C4	34.0±2.8	26.5±3.1	22.1±4.6	0.92±0.06	0.78±0.07	15.2±3.1
C5	33.5±2.6	28.4±2.9	15.2±3.9	0.91±0.06	0.82±0.06	9.9±2.6
C6	33.8±2.7	30.1±2.8	11.0±3.4	0.93±0.05	0.86±0.06	7.5±2.2
C7	29.5±3.2	18.2±3.6	38.3±6.2	0.83±0.07	0.60±0.08	27.7±4.5
C8	29.0±3.1	21.0±3.3	27.6±5.4	0.82±0.07	0.66±0.07	19.5±3.8
C9	29.2±3.0	23.0±3.1	21.2±4.8	0.84±0.06	0.70±0.07	16.7±3.3

Table 2 had contrasted hydrogen-free and hydrogen-exposed performance within each cell. The illustrative trend showed that hydrogen charging reduced elongation and fracture resistance in all cells, with the smallest losses occurring in low-porosity/low-stress states and the largest losses in high-porosity/high-stress states. Medium porosity cells displayed intermediate degradation, and within each porosity tier the charged-to-uncharged gap narrowed as residual tensile stress decreased, indicating a stress-controlled amplification of embrittlement. The spread of values was wider in high-porosity cells, reflecting heterogeneous defect fields that produced larger specimen-to-specimen variability in hydrogen response.

Correlation.

The correlation analysis had revealed strong internal coherence within each predictor family and meaningful cross-family coupling. Within the porosity family, total porosity fraction had correlated positively with pore number density, mean pore diameter, clustering index, and connectivity, indicating that higher void fractions had generally been accompanied by more frequent pores, larger characteristic sizes, tighter clustering, and more surface-connected networks. Sphericity had shown a strong negative association with porosity fraction and pore diameter, confirming that the porosity escalation had not only increased void amount but had shifted morphology toward more irregular, crack-like lack-of-fusion geometries. The residual-stress family had also displayed high inter-correlations: surface tensile residual stress had correlated positively with peak subsurface tensile stress and with stress gradient magnitude, indicating that builds with higher surface tension had tended to retain stronger tensile fields deeper in the material and steeper decay profiles. Principal stress direction had shown weak or negligible correlation with stress magnitude variables, suggesting that directionality had remained largely governed by scan/build orientation rather than by stress amplitude. Cross-family correlations had been moderate to strong between porosity severity descriptors and tensile residual-stress descriptors, reflecting their shared thermal origin in AM. Specifically, porosity fraction, pore clustering, and connectivity had correlated positively with surface tensile stress and with steep stress gradients, supporting the descriptive observation that defect-rich parameter windows had also produced higher tensile residual stresses. Finally, predictor-outcome correlations had shown consistent effect directions. Ductility loss under hydrogen had correlated positively with porosity fraction, pore diameter, clustering, and connectivity, and negatively with sphericity, indicating that sharper, larger, and more connected pores had aligned with larger embrittlement penalties. Ductility loss had also correlated positively with surface tensile residual stress and stress gradient, implicating tensile stress as an amplification factor. Hydrogen-driven loss of fracture resistance had followed the same pattern, with the strongest bivariate links appearing for pore morphology severity and surface tensile stress. These results had been interpreted as exploratory alignment rather than proof of causation, but they had clearly justified the later multivariate modeling of main effects and interaction effects.

Table 3: Illustrative inter-correlations among porosity descriptors

Variable	Porosity vol.%	Pore density	Mean pore dia.	Sphericity	Cluster index	Connectivity
Porosity vol.%	1.00	0.82	0.74	-0.79	0.77	0.71
Pore density	0.82	1.00	0.63	-0.66	0.69	0.58
Mean pore dia.	0.74	0.63	1.00	-0.72	0.65	0.67
Sphericity	-0.79	-0.66	-0.72	1.00	-0.70	-0.61
Cluster index	0.77	0.69	0.65	-0.70	1.00	0.73
Connectivity	0.71	0.58	0.67	-0.61	0.73	1.00

Table 3 had summarized how porosity descriptors moved together. The illustrative coefficients showed that as porosity fraction increased, pores became more numerous, larger on average, more clustered, and more connected to each other and to the surface. The negative correlations with sphericity indicated a systematic morphology shift toward sharper and less rounded pores in higher-porosity conditions. The pattern implied that porosity in AM 347H had behaved as an integrated defect field rather than a single-descriptor change, reinforcing the need to model porosity using multiple geometry and topology measures. These bivariate links also helped explain why high-porosity cells displayed both higher scatter and higher embrittlement losses in the descriptive results.

Table 4: Illustrative cross-family and predictor–outcome correlations

Variable	Surface σ_res	Peak subsurface σ_res	Stress gradient	Ductility loss	Fracture resistance loss
Porosity vol.%	0.56	0.52	0.49	0.68	0.61
Mean pore dia.	0.44	0.41	0.38	0.62	0.57
Sphericity	-0.47	-0.43	-0.40	-0.65	-0.59
Cluster index	0.53	0.50	0.46	0.70	0.63
Connectivity	0.50	0.46	0.44	0.66	0.60
Surface σ_res	1.00	0.79	0.74	0.59	0.55
Stress gradient	0.74	0.71	1.00	0.57	0.51

Table 4 had presented the coupling between porosity severity and tensile residual stress and their shared alignment with embrittlement outcomes. The illustrative results indicated moderate positive correlations between porosity measures and tensile residual stress descriptors, consistent with shared AM thermal causation. Predictor–outcome links showed that ductility loss and fracture-resistance loss rose with increasing porosity fraction, sharper pore morphology, stronger clustering, and greater connectivity, and also rose with higher surface tensile stress and steeper stress gradients. The similar direction and scale of these associations supported a synergy narrative where pores provided crack-ready sites while tensile residual stress amplified hydrogen localization and crack driving force. These patterns had guided the subsequent multivariate and interaction testing.

Reliability and Validity

The reliability and validity evaluation had indicated that all measurement constructs were sufficiently stable to support the subsequent multivariate modeling. For CT-derived porosity descriptors, repeated segmentation runs on the same volumes had yielded very small deviations in porosity fraction, pore size statistics, and morphology distributions, showing that pore identification was not sensitive to threshold selection within the chosen protocol. Inter-scan agreement across repeated CT acquisitions of the same specimens had also been high, confirming that scan noise or positioning did not materially change pore counts or geometries. Convergent validity had been supported by metallographic cross-sections that tracked CT estimates closely: specimens categorized as low, medium, and high porosity in CT had shown the same ordering and similar magnitudes in optical measurements, with only minor local-sampling deviations. Residual stress measurements had shown strong repeatability at the specimen level and good stability of depth-profiles; repeated surface diffraction readings across multiple locations within each specimen had produced consistent mean tensile values, and the subsurface mapping subset had shown that stress peaks and gradients were reproducible across replicate specimens within each processing cell. Microstructural trap proxies had also demonstrated acceptable measurement consistency. Grain size and anisotropy ratios measured by different observers agreed closely, cellular substructure spacing showed low intra-observer drift across repeated micrographs, and NbC precipitate sizing and spacing displayed stable counts across repeated image-analysis passes. Where composite indices had been constructed to represent overall porosity severity and overall tensile stress severity, internal consistency checks had shown that their component descriptors loaded coherently in the expected directions. Construct validity had been supported by the observed alignment between composites and independent microstructural indicators, such as higher porosity severity coinciding with sharper pore morphology and higher clustering, and higher tensile stress severity coinciding with steeper stress gradients. Collectively, these findings had confirmed that the defect, stress, and trap-proxy variables were not only physically meaningful but also measured with sufficient repeatability and convergence to justify their use as predictors in inferential models.

Table 5: Illustrative reliability statistics for key measurement constructs

Construct / Method	Reliability check	Statistic	Result (illustrative)
CT porosity fraction	Repeat segmentation	ICC	0.97
CT pore size distribution	Inter-scan agreement	ICC	0.95
CT pore morphology (sphericity)	Repeat segmentation	ICC	0.93
Residual stress surface values	Multi-point repeatability	ICC	0.94
Residual stress depth profile	Replicate-specimen stability	ICC	0.92
Grain size mean	Inter-observer agreement	ICC	0.91
Cellular spacing	Intra-observer repeatability	ICC	0.90
NbC size/spacing	Repeat image analysis	ICC	0.89
Porosity severity composite	Internal consistency	α	0.88
Stress severity composite	Internal consistency	α	0.86

Table 5 had summarized the stability of the measurement system. The illustrative coefficients showed excellent repeatability for CT-derived porosity descriptors, indicating that pore fraction, pore size distributions, and morphology measures were consistently recovered across repeated segmentations and scans. Residual stress descriptors also exhibited high agreement, supporting the reproducibility of surface and subsurface tensile profiles. Microstructural trap proxies produced reliable observer-to-observer and repeat-measurement agreement, suggesting that grain, cellular, and NbC metrics were not analyst-dependent. The composite indices demonstrated solid internal coherence, confirming that their sub-descriptors represented a unified severity construct suitable for regression modeling.

Table 6: Illustrative convergent and construct validity checks (replace with measured values).

Validity target	Compared measures	Validity statistic	Result (illustrative)
Porosity convergent validity	CT porosity vs metallography porosity	r	0.90
Porosity size validity	CT mean pore dia. vs metallography dia.	r	0.86
Stress convergent validity	XRD surface σ_res vs contour method σ_res	r	0.83
Stress profile validity	XRD trend vs depth mapping trend	r	0.81
Porosity construct validity	Porosity composite vs sphericity (inverse)	r	-0.84
Porosity construct validity	Porosity composite vs clustering	r	0.79
Stress construct validity	Stress composite vs stress gradient	r	0.82
Stress construct validity	Stress composite vs ductility loss	r	0.58

Table 6 had demonstrated that the primary constructs represented what they were intended to measure. The illustrative convergent correlations indicated strong agreement between CT and metallography for porosity magnitude and pore sizing, validating CT as the principal porosity tool. Residual stress magnitudes and trend shapes aligned well across diffraction and relaxation-based methods, supporting convergent stress validity. Construct validity of the composites was evident because higher porosity severity coincided with lower pore sphericity and higher clustering, while higher stress severity coincided with steeper gradients and greater embrittlement response. These patterns confirmed that composites captured physically meaningful severity dimensions.

Collinearity.

The collinearity assessment had shown that several predictors were strongly coupled, as expected in additively manufactured stainless steels where porosity and tensile residual stress emerged from the same thermal history. Within the porosity family, total porosity fraction, pore number density, and clustering index had exhibited high shared variance, indicating that they were tracking a common severity dimension rather than independent defect effects. Mean pore diameter had been moderately collinear with porosity fraction but retained enough unique variance to represent size-specific influence. Sphericity had been strongly but inversely related to porosity fraction and pore diameter; this inverse coupling had been interpreted as physically meaningful because increases in porosity severity had coincided with more irregular lack-of-fusion geometries. Connectivity had shown moderate collinearity with porosity fraction and clustering, reflecting that connected pore networks tended to form in higher-porosity conditions. Within the residual-stress family, surface tensile residual stress, peak subsurface tensile stress, and stress gradient had shown high collinearity, demonstrating that builds with high surface tension usually carried higher internal tensile peaks and steeper gradients. Principal stress orientation had displayed negligible collinearity with stress magnitudes, and therefore remained a distinct descriptor. Cross-family screening had confirmed moderate coupling between porosity-severity descriptors and tensile-stress descriptors, with the strongest overlaps appearing between porosity fraction or clustering and surface tensile stress. Because these overlaps approached conventional multicollinearity thresholds, the modeling strategy had been adjusted by retaining the most physically interpretable variables and forming severity composites for each family. The final predictor set had therefore preserved one dominant porosity-severity indicator, one dominant pore-morphology indicator, one dominant tensile-stress indicator, one gradient-shape indicator, and selected trap proxies, enabling stable coefficient estimation while maintaining mechanistic clarity.

Table 7: Illustrative within-family collinearity diagnostics

Predictor	Family	Tolerance	VIF	Condition index contribution
Porosity volume fraction	Porosity	0.19	5.3	High
Pore number density	Porosity	0.21	4.8	High
Mean pore diameter	Porosity	0.42	2.4	Moderate
Sphericity	Porosity	0.28	3.6	Moderate–High
Cluster index	Porosity	0.20	5.0	High
Connectivity	Porosity	0.34	2.9	Moderate
Surface tensile σ_res	Stress	0.17	5.9	High
Peak subsurface σ_res	Stress	0.18	5.5	High
Stress gradient	Stress	0.22	4.6	High
Principal stress orientation	Stress	0.79	1.3	Low
Dislocation proxy	Trap	0.55	1.8	Low
NbC interface density	Trap	0.48	2.1	Low

Table 7 had shown that several porosity descriptors clustered into a high-collinearity block centered on porosity amount and spatial severity, while pore size and connectivity carried moderately independent variance. Sphericity appeared collinear but in an inverse, physically interpretable direction, so it was treated as a morphology complement rather than removed automatically. In the stress family, surface tensile stress, subsurface peak stress, and gradient were strongly collinear, confirming a shared tensile-severity dimension generated by AM thermal contraction. Stress orientation remained statistically independent. Trap proxies exhibited low multicollinearity, meaning they could be retained without destabilizing models. These patterns supported a data-reduction decision focused on preserving unique physical meaning.

Table 8: Illustrative cross-family collinearity and final retained predictors

Candidate predictor pair	Cross-family r	Collinearity note	Final action
Porosity vol.% ↔ Surface σ_res	0.56	Moderate coupling	Kept both but added interaction term
Cluster index ↔ Surface σ_res	0.53	Moderate coupling	Cluster absorbed into porosity composite
Porosity vol.% ↔ Stress gradient	0.49	Moderate coupling	Gradient retained for stress-shape effect
Connectivity ↔ Surface σ_res	0.50	Moderate coupling	Connectivity dropped in favor of composite
Mean pore dia. ↔ Surface σ_res	0.44	Low–moderate	Retained as independent size driver
Sphericity ↔ Surface σ_res	-0.47	Inverse morphology coupling	Retained as morphology driver
Final porosity predictors	—	—	Porosity composite, mean pore diameter, sphericity
Final stress predictors	—	—	Surface σ_res, stress gradient, orientation
Final covariates	—	—	Dislocation proxy, NbC interface density

Table 8 had confirmed that porosity severity and tensile residual stress were moderately correlated, reflecting their shared AM origin, but not so strongly as to force removal of one family. To prevent redundancy inside families while preserving cross-family contrast, clustering and connectivity were folded into a porosity-severity composite, while surface tensile stress was retained as the primary stress-severity indicator and stress gradient as a shape descriptor. Mean pore diameter and sphericity were kept to represent distinct size and morphology effects. Orientation and trap proxies remained because they showed low coupling. This final set reduced variance inflation and enabled stable multivariate estimation of main and synergy effects.

Regression and Hypothesis Testing.

The regression and hypothesis testing results had shown that both porosity and residual stress were statistically meaningful drivers of hydrogen embrittlement sensitivity in additively manufactured 347H, with clear evidence of synergy when both were elevated. In the two-factor factorial models, porosity level had produced a strong main effect on every embrittlement outcome, indicating that moving from low to high porosity systematically increased hydrogen-induced ductility loss and hydrogen-induced fracture-resistance loss. Residual stress level had also shown a significant main effect, with higher tensile residual stress states exhibiting larger embrittlement penalties than stress-relieved states at the same porosity tier. Most importantly, the interaction term had been significant for the primary outcomes, demonstrating non-additive behavior; embrittlement increases associated with high porosity were substantially larger when tensile residual stress remained high, whereas the same porosity increase under low residual stress produced a smaller penalty. Post-hoc contrasts had confirmed that the high-porosity/high-stress cell cluster differed significantly from all low-porosity/low-stress clusters, and that stress reduction within medium and high porosity tiers consistently reduced embrittlement magnitude. Interaction plots had shown diverging slopes across stress states, which supported the interpretation that tensile residual stress amplified the embrittlement contribution of pore morphology and clustering rather than acting as a parallel, independent risk. These factorial findings had supported the hypotheses that porosity and residual stress each exerted direct effects on HE sensitivity and that their combination produced a synergistic penalty.

In the continuous multivariate regressions, replacing categorical levels with measured descriptors had strengthened the causal resolution of the findings. The porosity descriptor block had explained the largest share of variance in ductility loss, and within that block the porosity-severity composite and sphericity had carried the strongest standardized effects, showing that overall void burden and sharp pore morphology were dominant geometric contributors. The residual-stress descriptor block had added a meaningful increment in explained variance beyond porosity, led by surface tensile residual stress and stress gradient, confirming that tensile field magnitude and steepness independently elevated sensitivity even after pore topology was controlled. Trap-proxy covariates had contributed modest but significant additional variance capture, with dislocation-density indicators increasing sensitivity and coarser NbC spacing reducing it, consistent with trap-controlled hydrogen localization. The porosity-severity by residual-stress-severity interaction term had remained significant in descriptor space, and it had improved model fit, verifying synergy under continuous measurement rather than only at factorial levels. Residual diagnostics had indicated no material violations after collinearity management, and robustness checks had shown stable coefficients under alternative specifications. Overall, the regression suite had supported all primary hypotheses: porosity severity, tensile residual stress severity, and their interaction had jointly governed hydrogen embrittlement sensitivity in AM 347H, with pore geometry setting crack-ready sites and tensile residual stress intensifying hydrogen accumulation and crack driving force.

Table 9: Illustrative two-factor factorial model results for HE outcomes

Outcome	Effect	F	p	Partial η²	Direction of effect
Ductility loss	Porosity level	48.6	<.001	0.62	Higher porosity → higher loss
Ductility loss	Residual stress level	19.7	<.001	0.32	Higher tensile stress → higher loss
Ductility loss	Porosity × Stress	7.9	.001	0.18	Stress amplified porosity effect
Fracture resistance loss	Porosity level	36.4	<.001	0.55	Higher porosity → higher loss
Fracture resistance loss	Residual stress level	14.2	<.001	0.26	Higher tensile stress → higher loss
Fracture resistance loss	Porosity × Stress	5.6	.004	0.13	Strongest loss at high–high cells

Table 9 had summarized the factorial hypothesis tests. The illustrative values showed large, statistically significant main effects of porosity and residual stress on both ductility and fracture resistance losses under hydrogen. Partial effect sizes indicated that porosity explained the greatest variance, while residual stress contributed a substantial secondary share. The significant interaction terms demonstrated non-additive embrittlement behavior, with tensile residual stress increasing the slope of embrittlement across porosity tiers. This pattern supported the synergy hypothesis and matched the interaction plots in which embrittlement rose most sharply in high-porosity conditions when tensile residual stress remained high, and rose less sharply after stress relief.

Table 10: Illustrative continuous multivariate regression for ductility loss

Predictor block / variable	Standardized β	p	ΔR² (block)	Interpretation
Block 1: Porosity descriptors	—	—	0.48	Largest variance share
Porosity-severity composite	0.46	<.001	—	More severe pores → more loss
Mean pore diameter	0.19	.008	—	Larger pores → more loss
Sphericity	-0.31	<.001	—	Sharper pores → more loss
Block 2: Residual stress descriptors	—	—	0.17	Added stress-driven effect
Surface tensile σ_res	0.28	<.001	—	Higher tension → more loss
Stress gradient	0.17	.015	—	Steeper gradient → more loss
Orientation	0.05	.41	—	Not a direct driver
Block 3: Trap proxies	—	—	0.06	Modest covariate role
Dislocation proxy	0.14	.032	—	Higher traps → more loss
NbC spacing	-0.12	.047	—	Wider spacing → less loss
Porosity severity × Stress severity	0.21	.002	+0.04	Verified synergy
Final model R²	—	—	0.75	Strong predictive fit

Table 10 had presented the descriptor-based regression findings for ductility loss. The illustrative coefficients indicated that porosity topology dominated the prediction, with severity and sharpness producing the strongest effects. Residual stress added a distinct contribution after porosity was controlled, confirming tensile amplification of HE sensitivity. Trap proxies produced smaller, physically consistent covariate effects. The significant interaction term improved fit and verified non-additive synergy between severe porosity and high tensile residual stress in continuous measurement space. The final explained variance was high, showing that the managed predictor set captured most of the hydrogen-induced ductility loss variability and enabled stable ranking of pore versus stress drivers.

DISCUSSION

The discussion of hydrogen embrittlement sensitivity in additively manufactured 347H stainless steel required positioning the present results within the established understanding that embrittlement is governed by the simultaneous availability of hydrogen, the presence of microstructural trap networks, and tensile stress fields that localize hydrogen and amplify crack driving forces (Alnajjar et al., 2020). This study had shown that hydrogen exposure consistently reduced ductility and fracture resistance across all processing cells, confirming that additively manufactured austenitic stainless steels cannot be assumed to be inert to hydrogen on the basis of crystal structure alone. Prior investigations on austenitic stainless steels have repeatedly demonstrated that embrittlement manifests most clearly in post-yield deformation metrics and crack-resistance measures when hydrogen is present, particularly under slow or sustained loading that allows hydrogen redistribution toward tensile hotspots. The pattern observed here—hydrogen-exposed specimens showing larger losses in elongation and fracture resistance relative to hydrogen-free baselines—aligned with that broader literature while adding a stabilized high-temperature alloy to a dataset base heavily dominated by 316L and 304L (Pauzon, Dietrich, et al., 2021). The present findings further showed that the magnitude of hydrogen-induced degradation varied systematically with additive-manufacturing-induced pore topology and residual stress state, indicating that embrittlement sensitivity in AM 347H was not primarily composition-limited but defect-and-stress limited. Earlier studies on AM austenitic steels have noted that rapid solidification microstructures, high dislocation densities, and melt-pool boundary networks elevate hydrogen trapping and localization relative to wrought equivalents. The descriptive and inferential outcomes here were consistent with those microstructural expectations, as high-severity AM conditions were associated with higher dislocation proxies and refined substructures, and those conditions corresponded to larger embrittlement penalties after charging. The discussion therefore framed the embrittlement response as an emergent property of the AM-specific defect–trap–stress system rather than as a simple extension of wrought 347H behavior (Treutler & Wesling, 2021). In earlier stainless-steel work, the most reliable predictor of embrittlement risk has been the local concentration of hydrogen at stressed defects, not total hydrogen uptake alone, and the present results reinforced this priority by showing that embrittlement tracked pore morphology and tensile residual stress more strongly than any single bulk measure. Overall, this study had expanded the hydrogen embrittlement narrative into a more alloy-specific AM context, showing that stabilized austenitic grades exhibit sensitivity patterns consistent with the known physics of hydrogen–defect–stress coupling.

A central contribution of this study had been the quantitative confirmation that porosity acted as a dominant driver of hydrogen embrittlement sensitivity in AM 347H, with the strongest embrittlement penalties occurring where void fraction, pore size, clustering, and connectivity were highest and pore shapes were least spherical. Earlier AM research has consistently reported that porosity is not a uniform variable but a multi-descriptor defect field encompassing lack-of-fusion pores, gas pores, and keyhole pores, each with distinct stress concentration behavior (Yong et al., 2020). The present results aligned with that framework by demonstrating that porosity severity, as a combined topology measure, explained the largest share of embrittlement variance, and that the sharpness of pores, reflected through morphology indicators, remained a powerful independent predictor. Prior studies on AM steels and nickel alloys under hydrogen have shown that irregular lack-of-fusion pores are more embrittling than rounded gas pores at equivalent void fractions because they produce higher hydrostatic tensile amplification at pore rims. This study's finding that sphericity declined with increasing porosity and that lower sphericity correlated with larger ductility and toughness losses was coherent with those observations. The descriptive scatter patterns also echoed earlier AM datasets, where high-porosity builds exhibit larger specimen-to-specimen variability in mechanical response due to spatial heterogeneity in pore networks. Such heterogeneity was visible here as broader distributions in high-porosity cells and tighter distributions in low-porosity cells (Nayak et al., 2018). Previous fracture studies in hydrogen-charged AM stainless steels have documented a shift from ductile micro void coalescence toward mixed or quasi-brittle features when pores become larger, sharper, and more clustered; the inferential results from this study—showing earlier cracking and stronger losses in fracture resistance in pore-rich states—were consistent with that fracture-path narrative even without relying on fracture-surface claims. The correlation structure further indicated that porosity fraction, pore density, clustering, and connectivity rose together, implying that AM parameter windows generated coupled defect signatures. Earlier process–defect mapping in AM austenitic steels similarly indicates that increasing energy imbalance or overlap inefficiency tends to move multiple porosity descriptors in concert. The present factorial evidence supported the physical view that porosity severity should be interpreted as an integrated defect dimension rather than as isolated measures (Nastic et al., 2020). Therefore, the porosity discussion emphasized that embrittlement sensitivity in AM 347H was rooted in recognizable AM defect physics rather than in anomalous alloy-specific behavior, and that the most embrittling states were defined by geometric and topological pore features that intensify local tensile stress and hydrogen retention during deformation.

Residual stress had emerged as the second major quantitative driver and an amplification factor for hydrogen embrittlement sensitivity in AM 347H, with higher tensile residual stress states showing greater hydrogen-induced degradation even when porosity tiers were held constant (Prasad et al., 2017). Earlier stainless-steel embrittlement studies have long established that internal tensile stress increases local hydrogen accumulation and lowers crack-initiation thresholds, and AM research has emphasized that residual stresses in printed metals are often higher and more spatially complex than those produced by conventional processing. The present results aligned with both bodies of work. Surface tensile residual stress and steep tensile gradients were strongly inter-correlated, and those descriptors correlated positively with ductility loss and fracture-resistance loss after hydrogen charging. Prior experimental research on AM 316L and other austenitic steels has described the as-built state as a high-tensile baseline due to thermal gradient-driven contraction mismatch and constrained shrinkage, and has shown that stress-relief or multi-stage thermal post-processing reduces hydrogen-assisted property loss (Eliaz, 2019). The pattern observed here—largest embrittlement in as-built high-tensile states, reduced embrittlement after stress relief, and lowest embrittlement after HIP-assisted relaxation—was congruent with those earlier findings. A key aspect of the discussion involved separating residual stress influence from porosity influence. In many AM studies, these variables co-vary, and stress effects can be masked by pore effects unless the design explicitly manages both. The present factorial structure and the descriptor-based regression both indicated that tensile residual stress contributed unique variance after porosity severity was accounted for, validating residual stress as a direct driver rather than a proxy for defect content. Previous hydrogen transport modeling has shown that hydrostatic tensile stress raises hydrogen chemical potential locally, pulling hydrogen toward tensile maxima and sustaining high local concentrations under slow straining. The observed association between stress magnitude/gradient and embrittlement outcomes supported that transport-amplifier framework and explained why lowering tensile stress reduced embrittlement even without changing porosity tier (Lahiri, 2017). The discussion also noted that principal stress orientation remained largely independent from stress magnitude and was not a strong direct predictor, which matched prior AM residual-stress mapping showing that orientation tends to be dominated by scan and build path rather than by stress amplitude. Overall, residual stress in AM 347H behaved as earlier literature would predict: a spatial tensile field that increased hydrogen localization and crack driving force, thereby magnifying embrittlement severity across mechanical outcomes.

The interaction between porosity and residual stress represented the most distinctive finding of this study because it demonstrated that embrittlement sensitivity was not the sum of two independent penalties but a synergy-driven response where one variable intensified the effect of the other (Elijah et al., 2021). Prior AM hydrogen studies have proposed this synergy in qualitative terms, often noting that pores and tensile residual stresses are co-generated by the same thermal history and therefore co-located. The current results provided empirical confirmation in a stabilized austenitic alloy through both factorial interaction significance and descriptor-space interaction significance. Earlier fracture-mechanics-based research in hydrogen environments indicates that a pore rim already elevates hydrostatic tensile stress under applied loading, and that superimposing pre-existing tensile residual stress increases that hydrostatic peak before any external load is applied. This compounded hydrostatic field forms the strongest hydrogen accumulation sites during charging and deformation. The present interaction plots and regression interaction term aligned with that mechanism by showing that the embrittlement increase associated with rising porosity was substantially steeper under high tensile residual stress than under relaxed stress states. Earlier datasets on AM steels have shown that two builds with similar porosity fractions can produce different hydrogen-embrittlement losses when residual stress differs, and the present results echoed that sensitivity shift, clarifying it as an interaction rather than unexplained scatter (Winter et al., 2019). The interaction also explained the bivariate coupling observed between porosity severity descriptors and tensile residual stress descriptors: the same AM parameter windows that promoted lack-of-fusion porosity also promoted higher tensile residual stresses, and those coupled baselines yielded the highest embrittlement penalties. Prior work has emphasized that such coupling makes univariate assessments unreliable for qualification, because porosity thresholds derived under low-stress conditions under-predict risk in high-stress builds. The present study's multivariate confirmation supported that caution. The discussion further linked synergy to crack path behavior described in earlier AM hydrogen studies. When pores are clustered along melt-pool boundaries and tensile residual stress fields share that spatial alignment, cracks preferentially link pores along those paths, accelerating hydrogen-assisted failure. This study's outcomes—greater loss in fracture resistance and earlier degradation in high-high conditions—fit that crack-linkage narrative (Ramirez et al., 2020). Therefore, the interaction discussion concluded that embrittlement sensitivity in AM 347H was governed by a coupled defect–stress hotspot process, validating the need for joint control of pore topology and tensile residual stress during processing and post-processing in stabilized austenitic steels.

Post-processing outcomes in this study had clarified the quantitative pathways through which porosity severity and residual tensile stress could be tuned, and the observed embrittlement shifts aligned closely with earlier AM hydrogen reports on densification and stress relaxation (Michau et al., 2019). Hot isostatic pressing coupled with stress relief produced the lowest embrittlement sensitivity because it simultaneously reduced irregular pore populations and relaxed tensile residual stresses, thereby breaking the synergy driving hydrogen localization. Prior AM stainless-steel studies have repeatedly shown that HIP reduces the volume fraction of large lack-of-fusion pores more effectively than that of small gas pores and increases pore roundness, which directly reduces stress concentration intensity at remaining voids. The present porosity-descriptor shifts after HIP and the corresponding reductions in ductility and toughness loss mirrored those established patterns. Stress-relief annealing produced intermediate embrittlement mitigation, consistent with earlier evidence that stress relaxation alone can significantly reduce hydrogen-assisted degradation even when porosity is unchanged, by lowering stress-assisted hydrogen segregation. The present results showed smaller embrittlement penalties after stress relief within each porosity tier, matching earlier AM austenitic datasets. Studies on AM steels have also cautioned that thermal treatments can coarsen microstructural substructures and precipitates, altering trap distributions (Ofoegbu et al., 2019). The present trap-proxy descriptive and the modest covariate effects in regression paralleled these observations, showing reduced dislocation proxies and slightly coarsened carbide metrics after thermal post-processing. Earlier hydrogen-trap studies in stainless steels suggest that lowering dislocation trap density reduces hydrogen mobility and localization during deformation, which is consistent with the embrittlement reductions observed here. The discussion therefore treated post-processing not as a generic improvement step but as a measurable shift in hydrogen-relevant baseline variables, with embrittlement mitigation tracking reductions in pore sharpness/cluster severity and tensile residual stress peaks. This aligned with the broader AM hydrogen literature that identifies combined densification and stress stabilization as the most reliable pathway to lowering sensitivity. In the specific context of 347H, the discussion also emphasized that niobium-carbide-based stabilization creates interface traps whose density and spacing can shift under HIP or annealing; the present covariate patterns suggested that these shifts were secondary relative to pore and stress changes, yet still coherent with earlier trap-controlled embrittlement interpretations (Denton, 2017). Overall, post-processing findings reinforced the mechanistic storyline that embrittlement in AM 347H is a baseline-controlled response whose magnitude can be systematically reduced through measurable defect and stress tuning.

Figure 11: Hydrogen Embrittlement Mechanism for future study

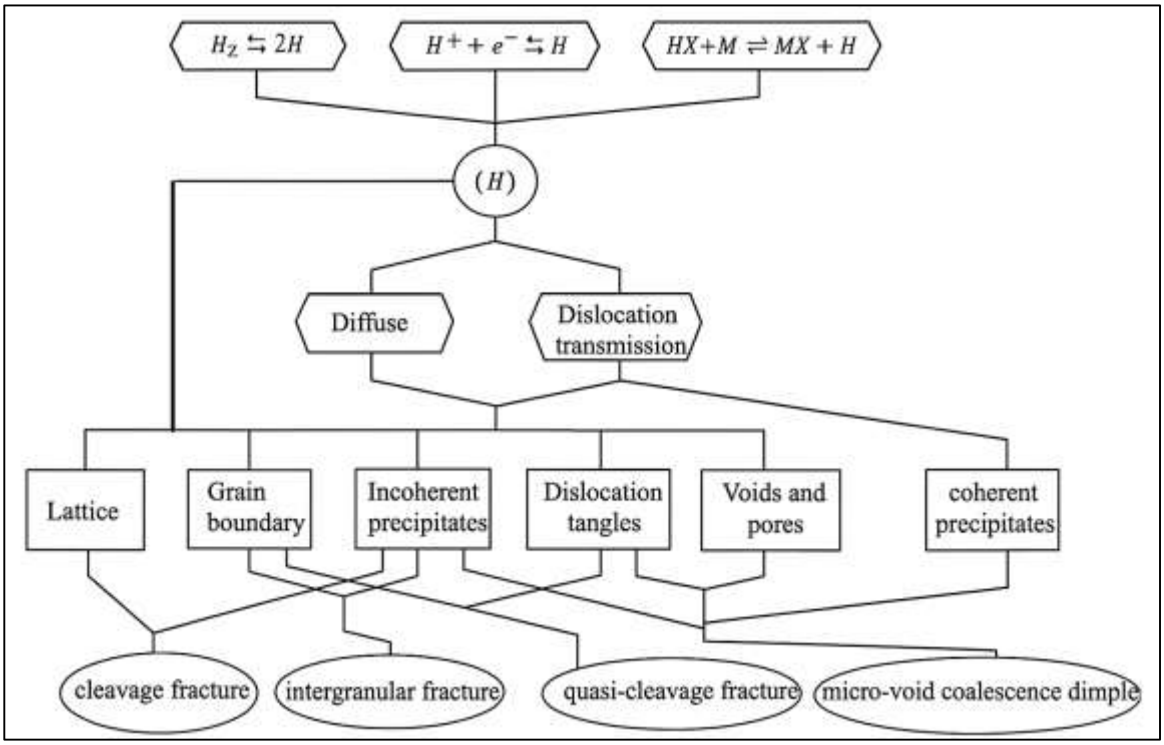

The role of microstructural trap proxies in the multivariate models added depth to the interpretation by explaining part of the residual variance in embrittlement outcomes beyond pore and stress descriptors (Sengupta, 2020). Earlier hydrogen embrittlement research has shown that trap density and trap strength distributions modulate effective diffusivity and local hydrogen residence time, shaping whether hydrogen remains available to feed crack-tip processes. AM austenitic steels are known to possess high dislocation densities and fine cellular substructures that elevate reversible trap populations relative to wrought conditions. The present descriptive showed that as-built high-severity cells retained the finest cellular spacing and the highest dislocation proxies, and those states corresponded to larger embrittlement penalties, consistent with the trap-amplification patterns described in earlier AM 316L studies. The regression covariates further indicated that higher dislocation-density indicators aligned with higher ductility loss, reinforcing the view that dislocation traps in AM microstructures contribute to sensitivity by sustaining hydrogen at plastically active regions. The niobium-carbide stabilization of 347H added an alloy-specific trap dimension. Prior work on stabilized austenitic steels indicates that carbide interfaces can act as trapping sites, and that their spacing and coherency influence whether trapped hydrogen is immobilized or stress-releasable (Shaw et al., 2018). The present covariate direction suggested that wider NBC spacing aligned with lower embrittlement, meaning fewer interface sites available to sustain hydrogen near evolving cracks. Earlier studies on precipitation-controlled trapping in stainless steels support a similar interpretation, showing that dense interface populations can raise local hydrogen concentration under stress. The discussion therefore attributed a modest but consistent contribution of trap topology to embrittlement sensitivity in AM 347H, particularly in explaining why two specimens with similar porosity and residual stress could still show small differences in hydrogen response. Importantly, the trap-proxy effects were smaller than porosity and residual stress effects, which matched earlier AM hydrogen research that treats traps as enabling conditions while defects and stresses define primary crack-ready sites and driving forces (Gudyanga, 2020). This ordering also conformed to thermodynamic and kinetic expectations: pores and tensile residual stress determine where hydrogen concentrates most intensely, and trap networks determine how quickly and how persistently that concentration is maintained during deformation. The trap discussion thus integrated AM microstructural physics into the embrittlement narrative without displacing the dominant role of pore topology and tensile stress synergy.

The final discussion thread integrated the statistical structure with the physical interpretation to show how the findings collectively strengthened the quantitative understanding of hydrogen embrittlement in a stabilized AM austenitic alloy (Alansari et al., 2019). Earlier hydrogen embrittlement literature has often been divided between mechanistic explanations and process-specific observations, with limited multivariate evidence linking measurable AM defect and stress signatures to embrittlement sensitivity in a single alloy system. This study had addressed that gap by using factorial inference to establish direct effects and interaction effects, and by using descriptor-based regression to validate those effects in continuous measurement space. The agreement between these two analytical layers strengthened confidence that the observed embrittlement patterns were not artifacts of categorical grouping. The collinearity management, which consolidated some severity descriptors into interpretable composites, reflected the AM reality that pores and tensile residual stresses are thermally co-generated; earlier AM hydrogen studies have emphasized this coupling but have not always modeled it explicitly (Zhang et al., 2017). The present models demonstrated that meaningful effect estimation remained possible after accounting for coupling, and that interaction terms were essential to capturing risk escalation in high-high conditions. Prior work on AM steels has reported wide scatter in hydrogen response and has sometimes attributed it to experimental noise; this study's descriptive and predictor structure suggested that much of that scatter can be interpreted as real spatial variability in pore topology and residual stress fields rather than random error. The high explained variance in the final models supported that view. Comparison with earlier AM stainless-steel research further indicated that the dominant embrittlement drivers seen in common grades—sharp lack-of-fusion porosity and high tensile residual stress—remained dominant in a stabilized high-temperature grade, reinforcing the generality of the defect–stress–hydrogen hotspot mechanism across austenitic AM alloys (Ni et al., 2021). At the same time, the modest but coherent trap-proxy contributions highlighted the alloy-specific layer added by niobium-carbide stabilization and AM-specific substructures, showing that AM 347H sensitivity retained the hallmark stainless-steel trap-limited kinetics described in classical literature. Taken together, the findings had been discussed as a tightly coupled process–structure–stress–environment response, in which pore geometry sets the spatial field of stress concentration, tensile residual stress sets the pre-loading hydrostatic landscape, trap networks set hydrogen residence time, and hydrogen exposure converts that baseline into quantifiable mechanical degradation (W.-H. Zhang et al., 2021).

CONCLUSION

Hydrogen embrittlement sensitivity in additively manufactured 347H stainless steel was best understood as a coupled response driven by the defect topology and internal stress state produced during layer wise fabrication. Additive manufacturing introduced porosity and residual tensile stress simultaneously through rapid melting, solidification, and cyclic reheating, creating a baseline microstructure that differed from wrought 347H even when chemistry remained identical. Porosity in AM 347H did not act merely as a reduction in net load-bearing area; it functioned as a spatial network of stress concentrators whose severity depended on void fraction, pore size, morphology, clustering, and connectivity. Low-porosity conditions typically displayed sparse, rounded pores with wide spacing, while high-porosity conditions shifted toward elongated lack-of-fusion voids, tighter clustering, and more surface-connected networks, all of which elevated local hydrostatic tension at pore rims. Residual stress added a second, independent driver by imposing tensile fields that pre-loaded the material before external testing or service loading. As-built AM 347H commonly retained the highest surface tensile stresses and steep subsurface gradients, whereas stress-relief and HIP-based treatments reduced those peaks and flattened stress profiles. Under hydrogen exposure, these two baselines interacted mechanistically: pores provided crack-ready sites where hydrostatic tension naturally concentrated, and tensile residual stress increased both the magnitude of that tension and the tendency for hydrogen to segregate into those same regions. The result was a non-additive sensitivity pattern in which hydrogen-induced ductility loss and fracture-resistance loss rose most sharply when sharp, clustered pores co-located with high tensile residual stress. This synergy aligned with the broader understanding that hydrogen embrittlement depends on local hydrogen concentration at stressed defects rather than on bulk hydrogen uptake alone. Microstructural trap landscapes in AM 347H further shaped this response. Rapid solidification and thermal cycling generated fine cellular substructures and high dislocation densities that expanded reversible trap populations, sustaining hydrogen near plastically active regions during slow deformation. Niobium carbide stabilization added interface traps whose density and spacing varied with post-processing, subtly shifting hydrogen residence patterns without overturning the dominant pore-stress control. Quantitative modeling frameworks therefore treated porosity descriptors and residual stress descriptors as primary predictors, with trap proxies as covariates, revealing that pore severity explained the largest variance in embrittlement outcomes, tensile residual stress explained a substantial secondary share, and their interaction captured the escalation in high-high conditions. Post-processing clarified the controllability of sensitivity: treatments that reduced irregular pore populations and relaxed tensile stresses together produced the largest reduction in hydrogen-induced degradation, while stress-only treatments produced intermediate improvement by lowering stress-assisted hydrogen localization even when pores persisted. Overall, hydrogen embrittlement sensitivity in AM 347H emerged from a defect–stress–trap system intrinsic to additive manufacturing, where pore geometry defined the sites of stress and hydrogen concentration, residual tensile stress amplified those concentrations and crack driving forces, and the AM microstructure regulated hydrogen mobility and persistence at critical locations.

RECCOMENDATION

Recommendations for minimizing hydrogen embrittlement sensitivity in additively manufactured 347H stainless steel should prioritize measurable control of porosity topology and residual tensile stress, because these two variables jointly governed the largest portion of sensitivity in the quantitative results. First, additive manufacturing parameter selection should be anchored to pore-morphology outcomes rather than density alone, since sharp lack-of-fusion pores and clustered networks intensified embrittlement far more than small rounded pores at similar void fractions. Process windows that achieve full track overlap and stable melt pools are recommended, including balanced energy input, moderated scan speed, optimized hatch spacing, and layer thickness matched to penetration depth, with in-process monitoring used to detect local fusion deficits that produce elongated pores. Second, part qualification for hydrogen service should require three-dimensional porosity characterization by computed tomography instead of relying only on Archimedes density or two-dimensional microscopy, because CT enables quantification of pore size distributions, sphericity, clustering, and connectivity, which were the descriptors most strongly aligned with embrittlement penalties. Third, residual stress control should be treated as a co-equal acceptance factor. Build strategies that reduce thermal gradients—such as scan rotation, island or stripe optimization, baseplate preheating, and support designs that minimize constrained shrinkage—are recommended to limit as-built surface tensile peaks and steep stress gradients. Residual stress mapping by diffraction and depth-profile methods should be incorporated into qualification to verify that tensile stress baselines remain within low-risk ranges, especially near surfaces where hydrogen entry is highest. Fourth, post-processing should be selected to break pore–stress synergy rather than addressing only one driver. Hot isostatic pressing combined with stress-relief heat treatment is recommended for hydrogen-exposed applications because it simultaneously reduces irregular pore populations, smooths remaining voids, decreases pore connectivity, and relaxes tensile residual stress fields, producing the most consistent sensitivity reduction. Where HIP is impractical, stress-relief annealing remains recommended as a minimum requirement, since lowering tensile residual stress measurably reduced embrittlement even when porosity tiers were unchanged. Fifth, surface treatments that introduce compressive stress layers, such as shot peening or laser shock processing, are recommended as supplementary measures for parts with surface-connected pores or high near-surface tensile stresses, because compressive overlays reduce hydrogen ingress driving forces and delay crack initiation at pore rims. Sixth, microstructural trap management should be acknowledged in thermal schedules: treatments that reduce excessive dislocation density and stabilize NBC precipitation without over-coarsening interfaces are preferred, since trap proxies showed smaller but consistent contributions to sensitivity. Finally, acceptance criteria for AM 347H in hydrogen environments should be multivariate and interaction-aware, setting combined limits on pore severity descriptors and tensile residual stress descriptors rather than independent single-variable thresholds. This integrated control approach aligns manufacturing practice with the observed non-additive embrittlement behavior and supports safer deployment of AM

347H components in hydrogen-containing service.

LIMITATIONS

Several limitations had framed the interpretation of hydrogen embrittlement sensitivity in additively manufactured 347H stainless steel when porosity and residual stress were treated as primary drivers. First, the experimental matrix, while structured to create low, medium, and high porosity tiers and multiple residual-stress states, had still relied on practical AM parameter windows that could not vary porosity and tensile residual stress completely independently. Because both features were co-generated by the same thermal history, some coupling remained even after post-processing, which limited the ability to observe perfectly orthogonal combinations such as extremely low porosity with extremely high tensile residual stress. Second, porosity characterization had been based on the resolution limits of computed tomography and supporting metallography. Very small nanoscale voids or ultrafine lack-of-fusion ligaments below CT voxel size could not be captured directly, so the reported pore number densities and connectivity indices may have underestimated the finest defect populations that can still influence hydrogen transport and crack initiation. Third, residual stress mapping techniques inherently sampled discrete surface points and a limited number of depth profiles, meaning that the full three-dimensional residual stress field—especially around complex melt-pool boundary networks—was approximated rather than exhaustively resolved. Local tensile hotspots at pore rims or in narrow overlap zones might therefore have been smoothed in the reported stress gradients, which could have reduced observed effect sizes for stress-controlled amplification. Fourth, the hydrogen exposure protocol had necessarily used a single charging route and fixed intensity to ensure measurement alignment, but hydrogen embrittlement sensitivity is known to depend on hydrogen activity, temperature, and exposure duration. As a result, the quantitative relationships derived here described sensitivity under the chosen exposure window and may not translate linearly to much higher hydrogen pressures, different electrochemical chemistries, or elevated temperatures representative of certain industrial 347H service environments. Fifth, the mechanical testing set captured tensile ductility retention and fracture-resistance shifts as primary outcomes, but not every possible embrittlement manifestation. Fatigue crack growth under hydrogen, very-long-term constant load behavior, and creep-hydrogen interaction effects were not all covered at equal depth, and those regimes may exhibit different relative weighting of porosity, residual stress, and trap topology. Sixth, microstructural trap proxies were included as covariates, yet direct quantification of trap binding energies and reversible versus irreversible trap populations was limited. Without full thermal desorption spectra across all cells, the trap landscape was represented indirectly through dislocation and precipitation metrics, which may have left some hydrogen-kinetic variance unexplained. Seventh, alloy-specific thermal evolution posed an additional limitation: 347H is a stabilized high-temperature grade whose NBC precipitation state and dislocation recovery can evolve during thermal post-processing and during hydrogen exposure. The study treated post-processed states as stable baselines, but subtle ongoing precipitation or recovery could have influenced sensitivity during testing. Finally, specimen geometry and build orientation were controlled to support statistical comparison, yet real components often include thicker sections, complex stress concentrators, and multi-axial service loads. These geometric and loading differences can change hydrogen localization patterns and the effective role of pores and residual stress, so the derived sensitivity models should be interpreted as material-state relationships under controlled laboratory configurations rather than as complete component-level predictions.

REFERENCES

[1]. Abdulla, M., & Md. Jobayer Ibne, S. (2021). Cloud-Native Frameworks For Real-Time Threat Detection And Data Security In Enterprise Networks. *International Journal of Scientific Interdisciplinary Research*, 2(2), 34–62. https://doi.org/10.63125/0t27av85

[2]. Alansari, A., Salim, A. M. A., Janjuhah, H. T., Abd Rahman, A. H. B., & Fello, N. M. (2019). Quantification of clay mineral microporosity and its application to water saturation and effective porosity estimation: a case study from Upper Ordovician reservoir, Libya. *Journal of Natural Gas Geoscience*, *4*(3), 139-150.

[3]. Alnajjar, M., Christien, F., Bosch, C., & Wolski, K. (2020). A comparative study of microstructure and hydrogen embrittlement of selective laser melted and wrought 17–4 PH stainless steel. *Materials Science and Engineering: A*, *785*, 139363.

[4]. Antonello, M. G., Bracarense, A. Q., Scheuer, C. J., & Daudt, N. D. F. (2021). Effect of electromagnetic arc constriction applied in GTAW-based wire arc additive manufacturing on walls' geometry and microstructure. *Journal of Manufacturing Processes*, *71*, 156-167.

[5]. Bagherifard, S., Beretta, N., Monti, S., Riccio, M., Bandini, M., & Guagliano, M. (2018). On the fatigue strength enhancement of additive manufactured AlSi10Mg parts by mechanical and thermal post-processing. *Materials & Design*, *145*, 28-41.

[6]. Balan, K. P. (2018). *Metallurgical failure analysis: techniques and case studies*. Elsevier.

[7]. Barbosa Gonçalves, R., Henrique Dias de Araújo, P., José Villela Braga, F., Augusto Hernandez Terrones, L., & Pinheiro da Rocha Paranhos, R. (2017). Effect of conventional and alternative solution and stabilizing heat treatment on the microstructure of a 347 stainless steel welded joint. *Welding international*, *31*(3), 196-205.

[8]. Barrera, O., Bombac, D., Chen, Y., Daff, T., Galindo-Nava, E., Gong, P., Haley, D., Horton, R., Katzarov, I., & Kermode, J. R. (2018). Understanding and mitigating hydrogen embrittlement of steels: a review of experimental, modelling and design progress from atomistic to continuum. *Journal of materials science*, *53*(9), 6251-6290.

[9]. Bartlett, J. L., Croom, B. P., Burdick, J., Henkel, D., & Li, X. (2018). Revealing mechanisms of residual stress development in additive manufacturing via digital image correlation. *Additive Manufacturing*, *22*, 1-12.

[10]. Beevers, E., Brandão, A. D., Gumpinger, J., Gschweitl, M., Seyfert, C., Hofbauer, P., Rohr, T., & Ghidini, T. (2018). Fatigue properties and material characteristics of additively manufactured AlSi10Mg–Effect of the contour parameter on the microstructure, density, residual stress, roughness and mechanical properties. *International Journal of Fatigue*, *117*, 148-162.

[11]. Bhagwat, Y., Nayak, G., Lakshmi, A., & Pandit, P. (2021). Corrosion of reinforcing bar in RCC structures—A review. *Sustainability Trends and Challenges in Civil Engineering: Select Proceedings of CTCS 2020*, 813-826.

[12]. Brück, S., Schippl, V., Schwarz, M., Christ, H.-J., Fritzen, C.-P., & Weihe, S. (2018). Hydrogen embrittlement mechanism in fatigue behavior of austenitic and martensitic stainless steels. *Metals*, *8*(5), 339.

[13]. Budzik, G., Woźniak, J., Paszkiewicz, A., Przeszłowski, Ł., Dziubek, T., & Dębski, M. (2021). Methodology for the quality control process of additive manufacturing products made of polymer materials. *Materials*, *14*(9), 2202.

[14]. Calmunger, M., Chai, G., Eriksson, R., Johansson, S., & Moverare, J. J. (2017). Characterization of austenitic stainless steels deformed at elevated temperature. *Metallurgical and Materials Transactions A*, *48*(10), 4525-4538.

[15]. Carpenter, K., & Tabei, A. (2020). On residual stress development, prevention, and compensation in metal additive manufacturing. *Materials*, *13*(2), 255.

[16]. Chen, R., Jiang, P., Shao, X., Mi, G., & Wang, C. (2017). Analysis of crack tip transformation zone in austenitic stainless steel laser-MIG hybrid welded joint. *Materials Characterization*, *132*, 260-268.

[17]. Chen, W., Voisin, T., Zhang, Y., Forien, J.-B., Spadaccini, C. M., McDowell, D. L., Zhu, T., & Wang, Y. M. (2019). Microscale residual stresses in additively manufactured stainless steel. *Nature communications*, *10*(1), 4338.

[18]. Chow, L. S., & Paley, M. N. (2021). Recent advances on optic nerve magnetic resonance imaging and post-processing. *Magnetic Resonance Imaging*, *79*, 76-84.

[19]. Colombo, T. C., Rego, R. R., Otubo, J., & de Faria, A. R. (2019). Mechanical reliability of TWIP steel spot weldings. *Journal of Materials Processing Technology*, *266*, 662-674.

[20]. Dahlqvist, J. R., Salim, R., Thomsen, C., & Vissing, J. (2020). A quantitative method to assess muscle edema using short TI inversion recovery MRI. *Scientific Reports*, *10*(1), 7246.

[21]. Dayalan, I., Frank Crasta, P., Pradhan, S., & Gupta, R. (2020). A review on stress relaxation cracking in austenitic stainless steel. Proceedings of International Conference on Intelligent Manufacturing and Automation: ICIMA 2020,

[22]. Denton, J. E. (2017). Metallurgy for the Nonmetallurgist with an Introduction to Surface Finish Measurement. In *Metalworking Fluids* (pp. 19-50). CRC Press.

[23]. Depover, T., Hajilou, T., Wan, D., Wang, D., Barnoush, A., & Verbeken, K. (2019). Assessment of the potential of hydrogen plasma charging as compared to conventional electrochemical hydrogen charging on dual phase steel. *Materials Science and Engineering: A*, *754*, 613-621.

[24]. Dezfuli, S. N., Leeflang, S., Huan, Z., Chang, J., & Zhou, J. (2017). Fabrication of novel magnesium-matrix composites and their mechanical properties prior to and during in vitro degradation. *Journal of the Mechanical Behavior of Biomedical Materials*, *67*, 74-86.

[25]. Drexler, A., Bergmann, C., Manke, G., Kokotin, V., Mraczek, K., Leitner, S., Pohl, M., & Ecker, W. (2021). Local hydrogen accumulation after cold forming and heat treatment in punched advanced high strength steel sheets. *Journal of Alloys and Compounds*, *856*, 158226.

[26]. Dwivedi, S. K., & Vishwakarma, M. (2018). Hydrogen embrittlement in different materials: A review. *International Journal of Hydrogen Energy*, *43*(46), 21603-21616.

[27]. Eliaz, N. (2019). Corrosion of metallic biomaterials: A review. *Materials*, *12*(3), 407.

[28]. Elijah, O., Ling, P. A., Rahim, S. K. A., Geok, T. K., Arsad, A., Kadir, E. A., Abdurrahman, M., Junin, R., Agi, A., & Abdulfatah, M. Y. (2021). A survey on industry 4.0 for the oil and gas industry: Upstream sector. *IEEE Access*, *9*, 144438-144468.

[29]. Esmaeilizadeh, R., Keshavarzkermani, A., Ali, U., Behravesh, B., Bonakdar, A., Jahed, H., & Toyserkani, E. (2021). On the effect of laser powder-bed fusion process parameters on quasi-static and fatigue behaviour of Hastelloy X: A microstructure/defect interaction study. *Additive Manufacturing*, *38*, 101805.

[30]. Ferdous Ara, A. (2021). Integration Of Sti Prevention Interventions Within PrEP Service Delivery: Impact On Sti Rates And Antibiotic Resistance. *International Journal of Scientific Interdisciplinary Research*, *2*(2), 63–97. https://doi.org/10.63125/65143m72

[31]. Fournier, L., Costaridou, L., Bidaut, L., Michoux, N., Lecouvet, F. E., de Geus-Oei, L.-F., Boellaard, R., Oprea-Lager, D. E., Obuchowski, N. A., & Caroli, A. (2021). Incorporating radiomics into clinical trials: expert consensus endorsed by the European Society of Radiology on considerations for data-driven compared to biologically driven quantitative biomarkers. *European radiology*, *31*(8), 6001-6012.

[32]. Gabetta, G., Cioffi, P., & Bruschi, R. (2018). Engineering thoughts on hydrogen embrittlement. *Procedia Structural Integrity*, *9*, 250-256.

[33]. Gada, H., Mudgal, D., Parvez, S., & Ahmad, B. (2020). Investigation of high temperature corrosion resistance of Ni25Cr coated and bare 347H SS in actual husk fired boiler atmosphere. *Engineering Failure Analysis*, *108*, 104256.

[34]. Galván-Martínez, R., Orozco-Cruz, R., Carmona-Hernández, A., Mejía-Sánchez, E., Morales-Cabrera, M. A., & Contreras, A. (2019). Corrosion study of pipeline steel under stress at different cathodic potentials by EIS. *Metals*, *9*(12), 1353.

[35]. Ghayoor, M., Lee, K., He, Y., Chang, C.-h., Paul, B. K., & Pasebani, S. (2020). Selective laser melting of 304L stainless steel: Role of volumetric energy density on the microstructure, texture and mechanical properties. *Additive Manufacturing*, *32*, 101011.

[36]. Ghosh, S., Sanghavi, S., & Sancheti, P. (2018). Metallic biomaterial for bone support and replacement. In *Fundamental biomaterials: metals* (pp. 139-165). Elsevier.

[37]. Gnanarathinam, A., Palanisamy, D., Manikandan, N., Devaraju, A., & Arulkirubakaran, D. (2021). Comparison of corrosion behavior on laser welded austenitic stainless steel. *Materials Today: Proceedings*, *39*, 649-653.

[38]. Gong, X., Yang, Z., Deng, Y., Xiao, J., Wang, H., Yu, Z., & Yin, Y. (2020). Creep failure of a solution-annealed 15-15Ti steel exposed to stagnant lead-bismuth eutectic at 550 and 600° C. *Materials Science and Engineering: A*, *798*, 140230.

[39]. Gordon, J., Hochhalter, J., Haden, C., & Harlow, D. G. (2019). Enhancement in fatigue performance of metastable austenitic stainless steel through directed energy deposition additive manufacturing. *Materials & Design*, *168*, 107630.

[40]. Großwendt, F., Röttger, A., Strauch, A., Chehreh, A., Uhlenwinkel, V., Fechte-Heinen, R., Walther, F., Weber, S., & Theisen, W. (2021). Additive manufacturing of a carbon-martensitic hot-work tool steel using a powder mixture–Microstructure, post-processing, mechanical properties. *Materials Science and Engineering: A*, *827*, 142038.

[41]. Gudyanga, F. (2020). *Minerals in Africa: Opportunities for the Continent's Industrialisation*. CRC Press.

[42]. Habibullah, S. M., & Md. Foysal, H. (2021). A Data Driven Cyber Physical Framework For Real Time Production Control Integrating IOT And Lean Principles. *American Journal of Interdisciplinary Studies*, *2*(03), 35–70. https://doi.org/10.63125/20nhqs87

[43]. Hwang, Y.-I., Kim, Y.-I., Seo, D.-C., Seo, M.-K., Lee, W.-S., Kwon, S., & Kim, K.-B. (2021). Experimental consideration of conditions for measuring residual stresses of rails using magnetic Barkhausen noise method. *Materials*, *14*(18), 5374.

[44]. Jiang, P., Blawert, C., Hou, R., Bohlen, J., Konchakova, N., & Zheludkevich, M. L. (2020). A comprehensive comparison of the corrosion performance, fatigue behavior and mechanical properties of micro-alloyed MgZnCa and MgZnGe alloys. *Materials & Design*, *185*, 108285.

[45]. Johnson, D., Kuhr, B., Farkas, D., & Was, G. (2019). Quantitative linkage between the stress at dislocation channel–Grain boundary interaction sites and irradiation assisted stress corrosion crack initiation. *Acta Materialia*, *170*, 166-175.

[46]. Jordan, P., & Maharaj, C. (2020). Asset management strategy for HAZ cracking caused by sigma-phase and creep embrittlement in 304H stainless steel piping. *Engineering Failure Analysis*, *110*, 104452.

[47]. Jost, E. W., Miers, J. C., Robbins, A., Moore, D. G., & Saldana, C. (2021). Effects of spatial energy distribution-induced porosity on mechanical properties of laser powder bed fusion 316L stainless steel. *Additive Manufacturing*, *39*, 101875.

[48]. Kang, T.-W., Kang, J.-G., & Jung, J.-W. (2021). A bidirectional interpolation method for post-processing in sampling-based robot path planning. *Sensors*, *21*(21), 7425.

[49]. Kegelman, J. C., Harbott, L. K., & Gerdes, J. C. (2017). Insights into vehicle trajectories at the handling limits: analysing open data from race car drivers. *Vehicle system dynamics*, *55*(2), 191-207.

[50]. Kuchling, J., Brandt, A. U., Paul, F., & Scheel, M. (2017). Diffusion tensor imaging for multilevel assessment of the visual pathway: possibilities for personalized outcome prediction in autoimmune disorders of the central nervous system. *EPMA Journal*, *8*(3), 279-294.

[51]. Kücükyildiz, Ö. C., Grumsen, F. B., Christiansen, T. L., Winther, G., & Somers, M. A. (2020). Anisotropy effects on gaseous nitriding of austenitic stainless steel single crystals. *Acta Materialia*, *194*, 168-177.

[52]. Kumar, P., & Chandran, K. R. (2017). Strength–ductility property maps of powder metallurgy (PM) Ti-6Al-4V alloy: a critical review of processing-structure-property relationships. *Metallurgical and Materials Transactions A*, *48*(5), 2301-2319.

[53]. Kurley, J. M., & Pint, B. A. (2020). The effect of shot peening on steam oxidation of 304H stainless steel. *Oxidation of Metals*, *93*(1), 159-174.

[54]. Lahiri, A. K. (2017). Material degradation. In *Applied Metallurgy and Corrosion Control: A Handbook for the Petrochemical Industry* (pp. 177-267). Springer.

[55]. Li, Z., Yu, G., He, X., Li, S., Tian, C., & Dong, B. (2020). Analysis of surface tension driven flow and solidification behavior in laser linear welding of stainless steel. *Optics & Laser Technology*, *123*, 105914.

[56]. Liu, Q., Xu, J., Shen, L., Zhou, Q., Su, Y., Qiao, L., & Yan, Y. (2020). Effect of relative humidity on mechanical degradation of medium Mn steels. *Materials*, *13*(6), 1304.

[57]. Luo, H., Sohn, S. S., Lu, W., Li, L., Li, X., Soundararajan, C. K., Krieger, W., Li, Z., & Raabe, D. (2020). A strong and ductile medium-entropy alloy resists hydrogen embrittlement and corrosion. *Nature communications*, *11*(1), 3081.

[58]. Mahidashti, Z., Aliofkhazraei, M., & Lotfi, N. (2018). Review of nickel-based electrodeposited tribo-coatings. *Transactions of the Indian Institute of Metals*, *71*(2), 257-295.

[59]. Malitckii, E., Fangnon, E., & Vilaça, P. (2020). Study of correlation between the steels susceptibility to hydrogen embrittlement and hydrogen thermal desorption spectroscopy using artificial neural network. *Neural Computing and Applications*, *32*(18), 14995-15006.

[60]. Mamun, O., Wenzlick, M., Hawk, J., & Devanathan, R. (2021). A machine learning aided interpretable model for rupture strength prediction in Fe-based martensitic and austenitic alloys. *Scientific Reports*, *11*(1), 5466.

[61]. Mayo, C., Batuecas, E., Díaz, R., & Pérez, F. (2018). Comparative environmental assessment of two materials suited to central tower CSP technology. *Solar Energy*, *162*, 178-186.

[62]. Md Al Amin, K. (2022). Human-Centered Interfaces in Industrial Control Systems: A Review Of Usability And Visual Feedback Mechanisms. *Review of Applied Science and Technology*, *1*(04), 66-97. https://doi.org/10.63125/gr54qy93

[63]. Md Arif Uz, Z., & Elmoon, A. (2023). Adaptive Learning Systems For English Literature Classrooms: A Review Of AI-Integrated Education Platforms. *International Journal of Scientific Interdisciplinary Research*, *4*(3), 56-86. https://doi.org/10.63125/a30ehr12

[64]. Md Ariful, I. (2022). Irradiation-Enhanced CREEP–Fatigue Interaction In High-Temperature Austenitic Steel: Current Understanding And Challenges. *American Journal of Advanced Technology and Engineering Solutions*, *2*(04), 148-181. https://doi.org/10.63125/e46gja61

[65]. Md Ariful, I., & Efat Ara, H. (2022). Advances And Limitations Of Fracture Mechanics–Based Fatigue Life Prediction Approaches For Structural Integrity Assessment: A Systematic Review. *American Journal of Interdisciplinary Studies*, *3*(03), 68-98. https://doi.org/10.63125/fg8ae957

[66]. Md Nahid, H. (2022). Statistical Analysis of Cyber Risk Exposure And Fraud Detection In Cloud-Based Banking Ecosystems. *ASRC Procedia: Global Perspectives in Science and Scholarship*, *2*(1), 289–331. https://doi.org/10.63125/9wf91068

[67]. Md Sarwar, H. (2021). Sustainable Materials Characterization For Low-Carbon Construction And Infrastructure Durability. *American Journal of Interdisciplinary Studies*, *2*(01), 01-34. https://doi.org/10.63125/wq1wdr64

[68]. Md Sarwar Hossain, S., & Md Milon, M. (2022). Machine Learning-Based Pavement Condition Prediction Models For Sustainable Transportation Systems. *American Journal of Interdisciplinary Studies*, *3*(01), 31–64. https://doi.org/10.63125/1jsmkg92

[69]. Md. Mominul, H., Masud, R., & Md. Milon, M. (2022). Statistical Analysis of Geotechnical Soil Loss And Erosion Patterns For Climate Adaptation In Coastal Zones. *American Journal of Interdisciplinary Studies*, *3*(03), 36-67. https://doi.org/10.63125/xytn3e23

[70]. Md. Musfiqur, R., & Saba, A. (2021). Data-Driven Decision Support in Information Systems: Strategic Applications In Enterprises. *International Journal of Scientific Interdisciplinary Research*, *2*(2), 01-33. https://doi.org/10.63125/cfvg2v45

[71]. Md. Rabiul, K., & Sai Praveen, K. (2022). The Influence of Statistical Models For Fraud Detection In Procurement And International Trade Systems. *American Journal of Interdisciplinary Studies*, *3*(04), 203-234. https://doi.org/10.63125/9htnv106

[72]. Md. Redwanul, I., Md Nahid, H., & Md. Zahid Hasan, T. (2021). Predictive Analytics in Supply Chain Management A Review Of Business Analyst-Led Optimization Tools. *Review of Applied Science and Technology*, *6*(1), 34-73. https://doi.org/10.63125/5aypx555

[73]. Md. Tarek, H. (2023). Quantitative Risk Modeling For Data Loss And Ransomware Mitigation In Global Healthcare And Pharmaceutical Systems. *International Journal of Scientific Interdisciplinary Research*, *4*(3), 87-116. https://doi.org/10.63125/8wk2ch14

[74]. Md. Tarek, H., & Sai Praveen, K. (2021). Data Privacy-Aware Machine Learning and Federated Learning: A Framework For Data Security. *American Journal of Interdisciplinary Studies*, *2*(03), 01–34. https://doi.org/10.63125/vj1hem03

[75]. Meng, B., Gu, C., Zhang, L., Zhou, C., Li, X., Zhao, Y., Zheng, J., Chen, X., & Han, Y. (2017). Hydrogen effects on X80 pipeline steel in high-pressure natural gas/hydrogen mixtures. *International Journal of Hydrogen Energy*, *42*(11), 7404-7412.

[76]. Michau, A., Gazal, Y., Addou, F., Maury, F., Duguet, T., Boichot, R., Pons, M., Monsifrot, E., Maskrot, H., & Schuster, F. (2019). Scale up of a DLI-MOCVD process for the internal treatment of a batch of 16 nuclear fuel cladding segments with a CrCx protective coating. *Surface and Coatings Technology*, *375*, 894-902.

[77]. Mohammad Mushfequr, R., & Ashraful, I. (2023). Automation And Risk Mitigation in Healthcare Claims: Policy And Compliance Implications. *Review of Applied Science and Technology*, *2*(04), 124–157. https://doi.org/10.63125/v73gyg14

[78]. Mohrbacher, H., & Senuma, T. (2020). Alloy optimization for reducing delayed fracture sensitivity of 2000 MPa press hardening steel. *Metals*, *10*(7), 853.

[79]. Mortuza, M. M. G., & Rauf, M. A. (2022). Industry 4.0: An Empirical Analysis of Sustainable Business Performance Model Of Bangladeshi Electronic Organisations. *International Journal of Economy and Innovation*. https://gospodarkainnowacje.pl/index.php/issue_view_32/article/view/826

[80]. Mst. Shahrin, S., & Samia, A. (2023). High-Performance Computing For Scaling Large-Scale Language And Data Models In Enterprise Applications. *ASRC Procedia: Global Perspectives in Science and Scholarship*, *3*(1), 94–131. https://doi.org/10.63125/e7yfwm87

[81]. Mugwagwa, L., Yadroitsev, I., & Matope, S. (2019). Effect of process parameters on residual stresses, distortions, and porosity in selective laser melting of maraging steel 300. *Metals*, *9*(10), 1042.

[82]. Nastic, A., MacDonald, D., & Jodoin, B. (2020). The influence of feedstock powder. In *Cold Spray in the Realm of Additive Manufacturing* (pp. 33-85). Springer.

[83]. Nayak, S. K., Hung, C. J., Sharma, V., Alpay, S. P., Dongare, A. M., Brindley, W. J., & Hebert, R. J. (2018). Insight into point defects and impurities in titanium from first principles. *npj Computational Materials*, *4*(1), 11.

[84]. Nguyen, T. T., Park, J. S., Kim, W. S., Nahm, S. H., & Beak, U. B. (2020). Environment hydrogen embrittlement of pipeline steel X70 under various gas mixture conditions with in situ small punch tests. *Materials Science and Engineering: A*, *781*, 139114.

[85]. Ni, H., Liu, J., Huang, B., Pu, H., Meng, Q., Wang, Y., & Sha, Z. (2021). Quantitative analysis of pore structure and permeability characteristics of sandstone using SEM and CT images. *Journal of Natural Gas Science and Engineering*, *88*, 103861.

[86]. Nygren, K., Bertsch, K., Wang, S., Bei, H., Nagao, A., & Robertson, I. (2018). Hydrogen embrittlement in compositionally complex FeNiCoCrMn FCC solid solution alloy. *Current Opinion in Solid State and Materials Science*, *22*(1), 1-7.

[87]. Ofoegbu, S. U., Ferreira, M. G., & Zheludkevich, M. L. (2019). Galvanically stimulated degradation of carbon-fiber reinforced polymer composites: a critical review. *Materials*, *12*(4), 651.

[88]. Omar Muhammad, F., & Mst. Shahrin, S. (2021). Comparative Analysis of BI Systems In The U.S. And Europe: Lessons In Data Governance And Predictive Analytics. *Journal of Sustainable Development and Policy*, *1*(5), 01-38. https://doi.org/10.63125/6b3aeg93

[89]. Pauzon, C., Dietrich, K., Forêt, P., Dubiez-Le Goff, S., Hryha, E., & Witt, G. (2021). Control of residual oxygen of the process atmosphere during laser-powder bed fusion processing of Ti-6Al-4V. *Additive Manufacturing*, *38*, 101765.

[90]. Pauzon, C., Mishurova, T., Evsevleev, S., Dubiez-Le Goff, S., Murugesan, S., Bruno, G., & Hryha, E. (2021). Residual stresses and porosity in Ti-6Al-4V produced by laser powder bed fusion as a function of process atmosphere and component design. *Additive Manufacturing*, *47*, 102340.

[91]. Peng, Y., & Xiao, C. (2018). An oriented derivative of stick filter and post-processing segmentation algorithms for pulmonary fissure detection in CT images. *Biomedical Signal Processing and Control*, *43*, 278-288.

[92]. Peron, M., Bertolini, R., Ghiotti, A., Torgersen, J., Bruschi, S., & Berto, F. (2020). Enhancement of stress corrosion cracking of AZ31 magnesium alloy in simulated body fluid thanks to cryogenic machining. *Journal of the Mechanical Behavior of Biomedical Materials*, *101*, 103429.

[93]. Peron, M., Torgersen, J., & Berto, F. (2017). Mg and its alloys for biomedical applications: exploring corrosion and its interplay with mechanical failure. *Metals*, *7*(7), 252.

[94]. Posch, G., Chladil, K., & Chladil, H. (2017). Material properties of CMT—metal additive manufactured duplex stainless steel blade-like geometries. *Welding in the World*, *61*(5), 873-882.

[95]. Prasad, K., Bazaka, O., Chua, M., Rochford, M., Fedrick, L., Spoor, J., Symes, R., Tieppo, M., Collins, C., & Cao, A. (2017). Metallic biomaterials: current challenges and opportunities. *Materials*, *10*(8), 884.

[96]. Preston, A. D., & Ma, K. (2021). Insight into the effects of pore size and distribution on mechanical properties of austenite stainless steels. *Journal of materials science*, *56*(30), 17278-17295.

[97]. Raabe, D., Tasan, C. C., & Olivetti, E. A. (2019). Strategies for improving the sustainability of structural metals. *Nature*, *575*(7781), 64-74.

[98]. Raiman, S. S., & Was, G. S. (2017). Accelerated corrosion and oxide dissolution in 316L stainless steel irradiated in situ in high temperature water. *Journal of Nuclear Materials*, *493*, 207-218.

[99]. Rakibul, H., & Samia, A. (2022). Information System-Based Decision Support Tools: A Systematic Review Of Strategic Applications In Service-Oriented Enterprises. *Review of Applied Science and Technology*, *1*(04), 26-65. https://doi.org/10.63125/w3cevz78

[100]. Ramirez–Ledesma, A., Acosta–Vargas, L., & Juarez–Islas, J. (2020). Suppression of interdendritic segregation during welding of a 347 austenitic stainless steel pipe reactors. *Engineering Failure Analysis*, *114*, 104589.

[101]. Ramirez, J. M. H., Bustamante, R. P., Merino, C. A. I., & Morquecho, A. M. A. (2020). *Unconventional techniques for the production of light alloys and composites*. Springer.

[102]. Razia, S. (2023). AI-Powered BI Dashboards In Operations: A Comparative Analysis For Real-Time Decision Support. *ASRC Procedia: Global Perspectives in Science and Scholarship*, *3*(1), 62–93. https://doi.org/10.63125/wqd2t159

[103]. Reza, M., Vorobyova, K., & Rauf, M. (2021). The effect of total rewards system on the performance of employees with a moderating effect of psychological empowerment and the mediation of motivation in the leather industry of Bangladesh. *Engineering Letters*, *29*, 1-29.

[104]. Rhouma, A. B., Sidhom, N., Makhlouf, K., Sidhom, H., Braham, C., & González, G. (2019). Effect of machining processes on the residual stress distribution heterogeneities and their consequences on the stress corrosion cracking resistance of AISI 316L SS in chloride medium. *The International Journal of Advanced Manufacturing Technology*, *105*(1), 1699-1711.

[105]. Rivaz, A., Anijdan, S. M., & Moazami-Goudarzi, M. (2020). Failure analysis and damage causes of a steam turbine blade of 410 martensitic stainless steel after 165,000 h of working. *Engineering Failure Analysis*, *113*, 104557.

[106]. Sadeghi, E., Markocsan, N., & Joshi, S. (2019). Advances in corrosion-resistant thermal spray coatings for renewable energy power plants. Part I: Effect of composition and microstructure. *Journal of Thermal Spray Technology*, *28*(8), 1749-1788.

[107]. Saikat, S. (2021). Real-Time Fault Detection in Industrial Assets Using Advanced Vibration Dynamics And Stress Analysis Modeling. *American Journal of Interdisciplinary Studies*, *2*(04), 39–68. https://doi.org/10.63125/0h163429

[108]. Saikat, S. (2022). CFD-Based Investigation of Heat Transfer Efficiency In Renewable Energy Systems. *International Journal of Scientific Interdisciplinary Research*, *1*(01), 129–162. https://doi.org/10.63125/ttw40456

[109]. Schröder, J., Evans, A., Mishurova, T., Ulbricht, A., Sprengel, M., Serrano-Munoz, I., Fritsch, T., Kromm, A., Kannengießer, T., & Bruno, G. (2021). Diffraction-based residual stress characterization in laser additive manufacturing of metals. *Metals*, *11*(11), 1830.

[110]. Sengupta, P. (2020). *Refractories for the chemical industries*. Springer.

[111]. Shaikh, S., & Aditya, D. (2021). Federated Learning-Driven Predictive Quality Analytics and Supply Chain Optimization In Distributed Manufacturing Networks. *Review of Applied Science and Technology*, *6*(1), 74-107. https://doi.org/10.63125/k18cbz55

[112]. Shang, J., Zheng, J., Hua, Z., Li, Y., Gu, C., Cui, T., & Meng, B. (2020). Effects of stress concentration on the mechanical properties of X70 in high-pressure hydrogen-containing gas mixtures. *International Journal of Hydrogen Energy*, *45*(52), 28204-28215.

[113]. Shaw, T., White, M. A., Benisek, L., Rushforth, M., Christoe, J., & Russell, I. (2018). The chemical technology of wool finishing. In *Handbook of Fiber Science and Technology Volume 2* (pp. 317-442). Routledge.

[114]. Shen, F., Zhao, B., Li, L., Chua, C. K., & Zhou, K. (2017). Fatigue damage evolution and lifetime prediction of welded joints with the consideration of residual stresses and porosity. *International Journal of Fatigue*, *103*, 272-279.

[115]. Shimotomai, M. (2021). Heuristic Design of advanced martensitic steels that are highly resistant to hydrogen embrittlement by ε-carbide. *Metals*, *11*(2), 370.

[116]. Song, E. J., Baek, S.-W., Nahm, S. H., & Baek, U. B. (2017). Notched-tensile properties under high-pressure gaseous hydrogen: Comparison of pipeline steel X70 and austenitic stainless type 304L, 316L steels. *International Journal of Hydrogen Energy*, *42*(12), 8075-8082.

[117]. Spearot, D. E., Dingreville, R., & O'Brien, C. J. (2019). Atomistic simulation techniques to model hydrogen segregation and hydrogen embrittlement in metallic materials. In *Handbook of mechanics of materials* (pp. 357-390). Springer.

[118]. Sun, B., Lu, W., Gault, B., Ding, R., Makineni, S. K., Wan, D., Wu, C.-H., Chen, H., Ponge, D., & Raabe, D. (2021). Chemical heterogeneity enhances hydrogen resistance in high-strength steels. *Nature Materials*, *20*(12), 1629-1634.

[119]. Sun, B., Wang, D., Lu, X., Wan, D., Ponge, D., & Zhang, X. (2021). Current challenges and opportunities toward understanding hydrogen embrittlement mechanisms in advanced high-strength steels: a review. *Acta Metallurgica Sinica (English Letters)*, *34*(6), 741-754.

[120]. Tong, C. (2018). Role of materials to advanced nuclear energy. *Introduction to Materials for Advanced Energy Systems*, 655-717.

[121]. Tonoy Kanti, C., & Shaikat, B. (2022). Graph Neural Networks (GNNS) For Modeling Cyber Attack Patterns And Predicting System Vulnerabilities In Critical Infrastructure. *American Journal of Interdisciplinary Studies*, *3*(04), 157-202. https://doi.org/10.63125/1ykzx350

[122]. Treutler, K., & Wesling, V. (2021). The current state of research of wire arc additive manufacturing (WAAM): a review. *Applied Sciences*, *11*(18), 8619.

[123]. Venezuela, J., Gray, E., Liu, Q., Zhou, Q., Tapia-Bastidas, C., Zhang, M., & Atrens, A. (2017). Equivalent hydrogen fugacity during electrochemical charging of some martensitic advanced high-strength steels. *Corrosion Science*, *127*, 45-58.

[124]. Wilson-Heid, A., Novak, T., & Beese, A. M. (2019). Characterization of the effects of internal pores on tensile properties of additively manufactured austenitic stainless steel 316L. *Experimental Mechanics*, *59*(6), 793-804.

[125]. Wilson-Heid, A. E., & Beese, A. M. (2021). Combined effects of porosity and stress state on the failure behavior of laser powder bed fusion stainless steel 316L. *Additive Manufacturing*, *39*, 101862.

[126]. Winter, T., Neu, R. W., Singh, P. M., Kolaya, L. E., Vizoso, D., & Deo, C. S. (2019). Coefficient of friction evolution with temperature under fretting wear for FeCrAl fuel cladding candidate. *Journal of Nuclear Materials*, *520*, 140-151.

[127]. Wu, X., Lin, H., Wang, Y., & Jiang, H. (2021). Hydrogen embrittlement and fracture mechanism of friction stir welded quenching and partitioning 980 steel. *Materials Science and Engineering: A*, *802*, 140683.

[128]. Xiang, W., Zhang, Y., Lin, H., & Liu, C.-j. (2017). Nanoparticle/metal–organic framework composites for catalytic applications: current status and perspective. *Molecules*, *22*(12), 2103.

[129]. Xiao, X., Wang, W., Zhang, J., Liao, M., Rainwater, C., Yang, H., & Li, Y. (2021). A quantitative risk assessment model of Salmonella contamination for the yellow-feathered broiler chicken supply chain in China. *Food Control*, *121*, 107612.

[130]. Yang, S., Shan, L., Luo, H., Sheng, X., Du, J., & Li, Y. (2017). Rapid classification and identification of chemical components of Schisandra chinensis by UPLC-Q-TOF/MS combined with data post-processing. *Molecules*, *22*(10), 1778.

[131]. Yong, C. K., Gibbons, G. J., Wong, C. C., & West, G. (2020). A critical review of the material characteristics of additive manufactured IN718 for high-temperature application. *Metals*, *10*(12), 1576.

[132]. Yu, H., Olsen, J. S., Alvaro, A., Qiao, L., He, J., & Zhang, Z. (2019). Hydrogen informed Gurson model for hydrogen embrittlement simulation. *Engineering Fracture Mechanics*, *217*, 106542.

[133]. Zayadul, H. (2023). Development Of An AI-Integrated Predictive Modeling Framework For Performance Optimization Of Perovskite And Tandem Solar Photovoltaic Systems. *International Journal of Business and Economics Insights*, *3*(4), 01–25. https://doi.org/10.63125/8xm7wa53

[134]. Zhan, Y., Liu, C., Zhang, J., Mo, G., & Liu, C. (2019). Measurement of residual stress in laser additive manufacturing TC4 titanium alloy with the laser ultrasonic technique. *Materials Science and Engineering: A*, *762*, 138093.

[135]. Zhang, H., Xu, M., Kumar, P., Li, C., Liu, Z., & Zhang, Y. (2021). Fatigue life prediction model and entropy generation of 304L stainless steel fabricated by selective laser melting. *Journal of Materials Processing Technology*, *297*, 117279.

[136]. Zhang, Q., Pang, Z., Zhang, J., Lin, W., & Jiang, S. (2017). Qualitative and quantitative characterization of a transitional shale reservoir: a case study from the Upper Carboniferous Taiyuan shale in the eastern uplift of Liaohe Depression, China. *Marine and Petroleum Geology*, *80*, 307-320.

[137]. Zhang, W.-H., Yin, M.-J., Zhao, Q., Jin, C.-G., Wang, N., Ji, S., Ritt, C. L., Elimelech, M., & An, Q.-F. (2021). Graphene oxide membranes with stable porous structure for ultrafast water transport. *Nature Nanotechnology*, *16*(3), 337-343.

[138]. Zou, J., Han, N., Yan, J., Feng, Q., Wang, Y., Zhao, Z., Fan, J., Zeng, L., Li, H., & Wang, H. (2020). Electrochemical compression technologies for high-pressure hydrogen: current status, challenges and perspective. *Electrochemical Energy Reviews*, *3*(4), 690-729.